

Planck early results: first assessment of the High Frequency Instrument in-flight performance

Planck HFI Core Team: P. A. R. Ade⁴⁷, N. Aghanim²⁵, R. Ansari³⁹, M. Arnaud³⁵, M. Ashdown^{33,54}, J. Aumont²⁵, A. J. Banday^{52,5,41}, M. Bartelmann^{51,41}, J. G. Bartlett^{1,31}, E. Battaner⁵⁷, K. Benabed²⁶, A. Benoit²⁶, J.-P. Bernard^{52,5}, M. Bersanelli^{15,20}, R. Bhatia¹⁷, J. J. Bock^{31,6}, J. R. Bond³, J. Borrill^{40,49}, F. R. Bouchet²⁶, F. Boulanger²⁵, T. Bradshaw⁴⁵, E. Bréelle¹, M. Bucher¹, P. Camus³⁸, J.-F. Cardoso^{36,1,26}, A. Catalano^{1,34}, A. Challinor^{55,33,7}, A. Chamballu²³, J. Charra^{25,†}, M. Charra²⁵, R.-R. Chary²⁴, C. Chiang¹¹, S. Church⁵⁰, D. L. Clements²³, S. Colombi²⁶, F. Couchot³⁹, A. Coulais³⁴, C. Cressiot¹, B. P. Crill^{31,43}, M. Crook⁴⁵, P. de Bernardis¹⁴, J. Delabrouille¹, J.-M. Delouis²⁶, F.-X. Désert²², K. Dolag⁴¹, H. Dole²⁵, O. Doré^{31,6}, M. Douspis²⁵, G. Efstathiou⁵⁵, P. Eng²⁵, C. Filliard³⁹, O. Forni^{52,5}, P. Fosalba²⁷, J.-J. Fourmond²⁵, K. Ganga^{1,24}, M. Giard^{52,5}, D. Girard³⁸, Y. Giraud-Héraud¹, R. Gispert^{25,†}, K. M. Górski^{31,59}, S. Gratton^{33,55}, M. Griffin⁴⁷, G. Guyot²¹, J. Haissinski³⁹, D. Harrison^{55,33}, G. Helou⁶, S. Henrot-Versillé³⁹, C. Hernández-Monteagudo⁴¹, S. R. Hildebrandt^{6,38,30}, R. Hills⁵⁶, E. Hivon²⁶, M. Hobson⁵⁴, W. A. Holmes³¹, K. M. Huffenberger⁵⁸, A. H. Jaffe²³, W. C. Jones¹¹, J. Kaplan¹, R. Kneissl^{16,2}, L. Knox¹², G. Lagache²⁵, J.-M. Lamarre^{34,*}, P. Lami²⁵, A. E. Lange^{24,†}, A. Lasenby^{54,33}, A. Lavabre³⁹, C. R. Lawrence³¹, B. Leriche²⁵, C. Leroy^{25,52,5}, Y. Longval²⁵, J. F. Macías-Pérez³⁸, T. Maciaszek⁴, C. J. MacTavish³³, B. Maffei³², N. Mandolesi¹⁹, R. Mann⁴⁶, B. Mansoux³⁹, S. Masi¹⁴, T. Matsumura⁶, P. McGehee²⁴, J.-B. Melin⁸, C. Mercier²⁵, M.-A. Miville-Deschênes^{25,3}, A. Moneti²⁶, L. Montier^{52,5}, D. Mortlock²³, A. Murphy⁴², F. Nati¹⁴, C. B. Netterfield¹⁰, H. U. Nørgaard-Nielsen⁹, C. North⁴⁷, F. Novello²⁵, D. Novikov²³, S. Osborne⁵⁰, C. Paine³¹, F. Pajot²⁵, G. Patanchon¹, T. Peacocke⁴², T. J. Pearson^{6,24}, O. Perdereau³⁹, L. Perotto³⁸, F. Piacentini¹⁴, M. Piat¹, S. Plaszczynski³⁹, E. Pointecouteau^{52,5}, R. Pons^{52,5}, N. Ponthieu²⁵, G. Prézeau^{6,31}, S. Prunet²⁶, J.-L. Puget²⁵, W. T. Reach⁵³, C. Renault³⁸, I. Ristorcelli^{52,5}, G. Rocha^{31,6}, C. Rosset¹, G. Roudier¹, M. Rowan-Robinson²³, B. Rusholme²⁴, D. Santos³⁸, G. Savini⁴⁴, B. M. Schaefer⁵¹, P. Shellard⁷, L. Spencer⁴⁷, J.-L. Starck^{35,8}, P. Stassi³⁸, V. Stolyarov⁵⁴, R. Stompor¹, R. Sudiwala⁴⁷, R. Sunyaev^{41,48}, J.-F. Sygnet²⁶, J. A. Tauber¹⁷, C. Thum²⁹, J.-P. Torre²⁵, F. Touze³⁹, M. Tristram³⁹, F. Van Leeuwen⁵⁵, L. Vibert²⁵, D. Vibert³⁷, L. A. Wade³¹, B. D. Wandelt^{26,13}, S. D. M. White⁴¹, H. Wiesemeyer²⁸, A. Woodcraft⁴⁷, V. Yurchenko⁴², D. Yvon⁸, and A. Zacchei¹⁸

(Affiliations can be found after the references)

October 29, 2018

Abstract

The *Planck* High Frequency Instrument (HFI) is designed to measure the temperature and polarization anisotropies of the Cosmic Microwave Background and galactic foregrounds in six wide bands centered at 100, 143, 217, 353, 545 and 857 GHz at an angular resolution of 10' (100 GHz), 7' (143 GHz), and 5' (217 GHz and higher). HFI has been operating flawlessly since launch on 14 May 2009. The bolometers cooled to 100 mK as planned. The settings of the readout electronics, such as the bolometer bias current, that optimize HFI's noise performance on orbit are nearly the same as the ones chosen during ground testing. Observations of Mars, Jupiter, and Saturn verified both the optical system and the time response of the detection chains. The optical beams are close to predictions from physical optics modeling. The time response of the detection chains is close to pre-launch measurements. The detectors suffer from an unexpected high flux of cosmic rays related to low solar activity. Due to the redundancy of *Planck*'s observation strategy, the removal of a few percent of data contaminated by glitches does not significantly affect the sensitivity. The cosmic rays heat up the bolometer plate and the modulation on periods of days to months of the heat load creates a common drift of all bolometer signals which do not affect the scientific capabilities. Only the high energy cosmic ray showers induce inhomogeneous heating which is a probable source of low frequency noise. The removal of systematic effects in the time ordered data provides a signal with an average level of noise less than 70% of our goal values in the 0.6–2.5 Hz range. This is slightly higher than the pre-launch measurements but better than predicted in the early phases of the project. This is attributed to the low level of photon noise resulting from an optimized optical and thermal design.

Key words. Methods: data analysis – Cosmology: observations

1. Introduction

*Planck*¹ (Tauber et al. 2010a; Planck Collaboration 2011a)

* Corresponding author: J.-M. Lamarre, jean-michel.lamarre@obspm.fr.

¹ *Planck* (<http://www.esa.int/Planck>) is a project of the European Space Agency (ESA) with instruments provided by two scientific consortia funded by ESA member states (in par-

is the third-generation space mission to measure the anisotropy of the cosmic microwave background (CMB). It observes the sky in nine frequency bands covering 30–

ticular the lead countries France and Italy), with contributions from NASA (USA) and telescope reflectors provided by a collaboration between ESA and a scientific consortium led and funded by Denmark.

857 GHz with high sensitivity and angular resolution from 31' to 5'. The Low Frequency Instrument (LFI; [Mandolesi et al. 2010](#); [Bersanelli et al. 2010](#); [Mennella et al. 2011](#)) covers the 30, 44, and 70 GHz bands with amplifiers cooled to 20 K. The High Frequency Instrument (HFI; [Lamarre et al. 2010](#); [Planck HFI Core Team 2011a](#)) covers the 100, 143, 217, 353, 545, and 857 GHz bands with bolometers cooled to 0.1 K. Polarization is measured in all but the highest two bands ([Leahy et al. 2010](#); [Rosset et al. 2010](#)). A combination of radiative cooling and three mechanical coolers provides the temperatures needed for the detectors and optics ([Planck Collaboration 2011b](#)). Two data processing centres (DPCs) check and calibrate the data and make maps of the sky ([Planck HFI Core Team 2011b](#); [Zacchei et al. 2011](#)). *Planck*'s sensitivity, angular resolution, and frequency coverage make it a powerful instrument for galactic and extragalactic astrophysics as well as cosmology. Early astrophysics results are given in [Planck Collaboration \(2011h–x\)](#).

The goal of this paper is to describe the in-flight performance of the HFI in space and after the challenging launch conditions. It does not attempt to duplicate the content of the *Planck* pre-launch status papers ([Lamarre et al. 2010](#); [Pajot et al. 2010](#)), but rather presents the operational status from an instrumental viewpoint. These results propagate to scientific products through the data processing reported in the companion paper ([Planck HFI Core Team 2011b](#)) which describes the instrumental properties as they appear in the maps used by the “*Planck* early results” companion papers. This paper focuses on the ability of the HFI to measure intensity without any description of its performance in measuring polarization, which will be reported later.

Section 2 summarizes the instrument design. Section 3 focuses on early in-flight operations, the verification phase and the setting of the parameters that have to be tuned in flight. Section 4 addresses the measurement of the beams on planets and the disentangling of time response effects from the beam shape. It also presents the best current knowledge of the physical beams resulting from this work. The effective beam obtained after data processing are to be found in [Planck HFI Core Team \(2011b\)](#). Sections 5, 6 and 7 are dedicated to noise, systematic effects and instrument stability respectively. A summary of the HFI in-flight performance and a comparison with pre-launch expectations are presented in section 8.

2. The HFI instrument

2.1. Design

The High Frequency Instrument (HFI) was proposed to ESA in response to the announcement of opportunity for instruments for the *Planck* mission in 1995. It is designed to measure the sky in six bands (Tab. 1) with bolometer sensitivity close to the fundamental limit set by photon noise. The lower four frequency bands include the measurement of the polarization. This sensitivity is obtained through a combination of technological breakthroughs in each of the critical components needed for bolometric detection:

- Spider web bolometers ([Bock et al. 1995](#); [Holmes et al. 2008](#)) and polarization sensitive bolometers ([Jones et al. 2003](#)) which can reach the photon noise limit with sufficient bandwidth to enable scanning great circles on

the sky at roughly 1 rpm. They offer a very low cross-section to cosmic rays that proves to be essential in this environment and with this sensitivity.

- A space qualified 100 mK dilution cooler ([Benoît et al. 1997](#)) associated with a high precision temperature control system.
- An active cooler for 4 K ([Bradshaw & Orłowska 1997](#)) using vibration controlled mechanical compressors to prevent excessive warming of the 100 mK stage and minimize parasitic effects on bolometers.
- AC biased readout electronics that extend high sensitivity to very slow signals ([Gaertner et al. 1997](#)).
- A thermo-optical design consisting, for each optical channel, of three corrugated horns and a set of compact reflective filters and lenses at cryogenic temperatures ([Church et al. 1996](#)). These include high throughput (multimoded) corrugated horns for the 545 and 857 GHz channels ([Murphy et al. 2002](#)).

The angular resolution was chosen to extend the measurement of the small scale features in the CMB, while keeping the level of stray light to extremely low levels. At the same time, at this sensitivity, the measurement and removal of foregrounds requires a large number of bands extending on both sides of the foreground minimum. This is achieved with the six bands of the HFI (Table 1) and the three bands of the Low Frequency Instrument (LFI; [Mennella et al. 2011](#)).

The instrument uses a ~ 20 K sorption cooler common to the HFI and the LFI ([Planck Collaboration 2011b](#); [Bhandari et al. 2000, 2004](#)). The HFI focal plane unit (FPU) is integrated inside the mechanical structure of the LFI, on axis of the focal plane of a common telescope ([Tauber et al. 2010a](#)).

The ability to achieve background limited sensitivity was demonstrated by the ARCHEOPS balloon-borne experiment ([Benoît et al. 2003a,b](#)), an adaptation of the HFI designed for operation in the environment of a stratospheric balloon. Similarly, the method of polarimetry employed by the HFI was demonstrated by the Boomerang experiment ([Montroy et al. 2006](#); [Piacentini et al. 2006](#); [Jones et al. 2006](#)). The HFI itself was extensively tested on the ground during the calibration campaigns ([Pajot et al. 2010](#)) at IAS in Orsay and CSL at Liège. However, the fully integrated instrument was never characterized in an operational environment like that of the second Earth-Sun Lagrange point (L2). In addition to thermal and gravitational environmental conditions, the spectrum and flux of cosmic rays at L2 is vastly different than that during the pre-flight testing. Finally, due to the operational constraints of the cryogenic receiver, the end to end optical assembly could not be tested on the ground with the focal plane instruments.

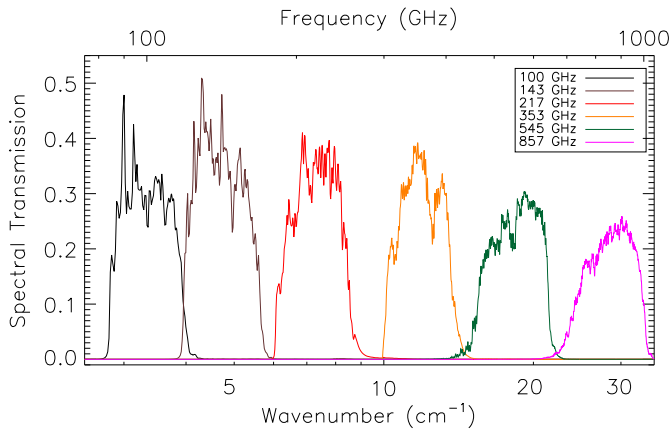
The instrument design and development are described in [Lamarre et al. \(2010\)](#). The calibration of the instrument is described in [Pajot et al. \(2010\)](#). The overall thermal and cryogenic design and the *Planck* payload performance are critical aspects of the mission. Detailed system-level aspects are described in [Planck Collaboration \(2011a\)](#) and [Planck Collaboration \(2011b\)](#).

2.2. Spectral transmission

The spectral calibration is described in [Pajot et al. \(2010\)](#) and consists of pre-launch data, in the passband and

Table 1. The HFI receivers. P stands for polarisation sensitive bolometers.

Channel		100P	143P	143	217P	217	353P	353	545	857
Central frequency	(GHz)	100	143	143	217	217	353	353	545	857
Bandwidth	(%)	33	32	30	29	33	29	28	31	30
Number of bolometers		8	8	4	8	4	8	4	4	4

**Figure 1.** HFI spectral transmission

around, combined with component level data to determine the out of band rejection over an extended frequency range (radio–UV). Analysis of the in-flight data shows that the contribution of CO rotational transitions to the HFI measurements is important. An evaluation of this contribution for the $J = 1 \rightarrow 0$ (100 and 143 GHz), $J = 2 \rightarrow 1$ (217 GHz) and $J = 3 \rightarrow 2$ (353 GHz) transitions of CO is presented in [Planck HFI Core Team \(2011b\)](#).

3. Early HFI operation

3.1. HFI Cool down and cryogenic operating point

The *Planck* satellite cooldown is described in [Planck Collaboration \(2011b\)](#).

The first two weeks after launch were used for passive outgassing, which ended on 2 June 2009. During this period, gas was circulated through the ^4He -JT cooler and the dilution cooler to prevent clogging by condensable gases. The sorption cooler thermal interface with HFI reached a temperature of 17.2 K on 13 June. The ^4He -JT cooler was only operated at its nominal stroke amplitude of 3.5 mm on 24 June to leave time for the LFI to carry out a specific calibration with their reference loads around 20 K. The operating temperature was reached on 27 June, with the thermal interface with the focal plane unit at 4.37 K.

The dilution cooler cold head reached 93 mK on 3 July 2009. Taking into account the specific LFI calibration requirement that slowed down the cooldown, the system behaved as expected within a few days, according to the thermal models adjusted to the full system cryogenic tests in the summer 2008 at CSL (Liège).

The regulated operating temperature point of the 4 K stage was set at 4.8 K for the 4 K feed horns on the FPU. The other stages were set to 1.395 K for the so called 1.4 K stage, 100.4 mK for the regulated dilution plate, and 103 mK for the bolometer regulated plate.

These numbers were very close to the planned operating point. As the whole system worked nominally, margins on the cooling chain for interface temperatures and heat lift are large. The *Planck* active cooling chain was one of the great technological challenges of this mission and is fully successful. A full description of the performance of the cryogenic chain and its system aspects can be found in [Planck Collaboration \(2011b\)](#). The parameters of the operating points of the 4 K, 1.4 K and 100 mK stages are summarised in [Table 2](#).

The temperature stability of the regulated stages has a direct impact on the scientific performance of the HFI. These stabilities are discussed in detail in [Planck Collaboration \(2011b\)](#). Their impact on the power received by the detectors is given in [Sect. 3.3.1](#).

3.2. Calibration and performance verification phase

3.2.1. Overview

The calibration and performance verification (CPV) phase of the HFI consisted of activities during the initial cooldown to 100 mK and during a period of about six weeks before the start of the survey. The cooldown phase is summarized in [Sect. 3.1](#). The pre-launch value of the ^4He -JT cooler operating frequency was used (see [Sect. 3.2.2](#)). Activities related to the optimization of the detection chain settings were performed first during the cooldown of the JFET amplifiers, and again when the bolometers were at their operating temperature. Most of the operating conditions were pre-determined during the ground calibration. The main unknown was the in-flight background on the detectors. The detection chain settings are presented in [Sect. 3.2.3](#). Other CPV activities performed are:

- determination of the detection chain time response under the flight background
- determination of the detection chain channel-to-channel crosstalk under the flight background
- characterization of the bolometer response to the 4 K and 1.4 K optical stages, and to the bolometer plate temperature variations
- checking the immunity of the instrument to the satellite transponder
- optimization of the numerical compression parameters for the actual sky signal and high energy particle glitch rate
- various ring-to-ring slew angles (1/7, 2/0 [nominal], 2/5)
- checking the effect of the scan angle with respect to the Sun
- checking the effect of the satellite spin rate around its nominal value of 1 rpm.

On 5 August 2009, an unexpected shutdown of the ^4He -JT cooler was triggered by its current regulator unit (CRU). Despite investigations into this event, its origin is still unexplained. A procedure for a quick restart was developed

Table 2. Main operation and interface parameters of the cooling chain

Interface Sorption cooler- ⁴ He-JT cooler (4 K gas pre-cooling temperature)	17.2 K
Interface ⁴ He-JT cooler-dilution cooler (dilution gas pre-cooling temperature)	4.37 K
Interface 1.4 K cooler-dilution gas precooling	1.34 K
Temperature of dilution plate (after regulation)	100.4 mK
Temperature of bolometer plate (after regulation)	103 mK
Temperature of 1.4 K plate (after regulation)	1.395 K
Temperature of 4 K plate (after regulation)	4.80 K
Dilution plate PID power	24.3–30.7 nW
Bolometer plate PID power	5.1–7.4 nW
1.4 K PID power	270 μ W
4 K PID power	1.7 mW
⁴ He-JT cooler stroke amplitude	3450 μ m
Dilution cooler ⁴ He flow rate	16.19–16.65 μ mole/s
Dilution cooler ³ He flow rate	5.92–6.00 μ mole/s
Present survey life time (started 6 August 2009)	29.4 months

and implemented in case the problem recurred, but it has not. Six days were required to re-cool the instrument to its operating point. The two-week first light survey (FLS) followed this recovery, starting on 15 August 2009. The FLS allowed assessment of the quality of the instrument settings, readiness of the data processing chain, and satellite scanning before the start of science operations. The complete instrument and satellite settings were validated and kept, and science operations began. All activities performed during the CPV phase confirmed the pre-launch estimates of the instrument settings and operating mode. We will detail in the following paragraphs the most significant ones.

3.2.2. ⁴He-JT cooler operating frequency setting

The ⁴He-JT cooler operating frequency was set to the nominal value of 40.08 Hz determined during ground tests. Once the cryochain stabilized, the in-flight behaviour of the cooler was found to be very similar to that observed during ground tests. The lines observed in the signal due to known electromagnetic interference (EMI) from the ⁴He-JT cooler drive electronics have the same very narrow width. The long term evolution of the ⁴He-JT cooler parasitic lines is discussed in Sect. 6.

3.2.3. Detection chain parameters setting

The JFET preamplifiers are operated at the temperature which minimizes their noise. This setting was checked when the bolometers were still warm (above 100 K) during the cooldown, since the bolometer Johnson noise was then much lower than the JFET noise. Optimum noise performance of the JFETs was found close at 130 K, in agreement with the ground calibration.

After ground calibration, the only parameters of the REU remaining to optimize in-flight were the bolometer bias current and the phase of the lock-in detection, which slightly depends on the bolometer impedance. Fig. 2 shows the bolometer responses for a set of bias current values measured while *Planck* was scanning the sky. For this sequence, the satellite rotation axis was fixed. For each bias value, the total detection chain noise was computed after subtraction of the sky signal. Ground measurements have shown that the minimum NEP and the maximum responsivity bias currents differ by less than 1%. Because of its

higher signal-to-noise ratio, we use the responsivity to optimize the bias currents (Catalano et al. 2010). The optimum in-flight bias current values correspond to the pre-launch estimates within 5%. Therefore the pre-launch settings, for which extensive ground characterizations were performed, were kept (Fig. 2). In a similar way, the lock-in phase was explored and optimized, and again the pre-launch settings were kept.

The optical background power on the bolometers is on the low end of our rather conservative range of predictions, even lower than expected from the ground measurements. This is attributed to a low telescope temperature and no detectable contamination of the telescope surface by dust during launch. This should result in a level of photon noise lower than initially expected and an improved sensitivity.

3.2.4. Numerical data-compression tuning

The output of the readout electronic unit (REU) consists of one number for each of the 72 science channels for each half-period of modulation (Lamarre et al. 2010). This number, S_{REU} , is the exact sum of the 40 16-bit ADC signal values obtained within the given half-period. The data processor unit (DPU) performs a lossy quantization of S_{REU} .

First, 254 S_{REU} values corresponding to about 1.4 s of observation for each detector, covering a strip of sky about 8° long, are processed. These 254 values are called a *compression slice*. The mean $\langle S_{REU} \rangle$ of the data within each compression slice is computed, and data are demodulated using this mean:

$$S_{demod,i} = (S_{REU,i} - \langle S_{REU} \rangle) * (-1)^i \quad (1)$$

where $1 < i < 254$ is the running index within the compression slice.

Then the mean $\langle S_{demod} \rangle$ of the demodulated data $S_{demod,i}$ is computed and subtracted. The resulting data slice is quantized according to a step Q fixed per detector:

$$S_{DPU,i} = \text{round}((S_{demod,i} - \langle S_{demod} \rangle)/Q) \quad (2)$$

This is the lossy part of the algorithm: the required compression factor, obtained through the tuning of the quantization step Q , adds some extra noise to the data. For $\sigma/Q = 2$, where σ is the standard deviation of Gaussian white noise, the quantization adds 1% to the noise (Pajot

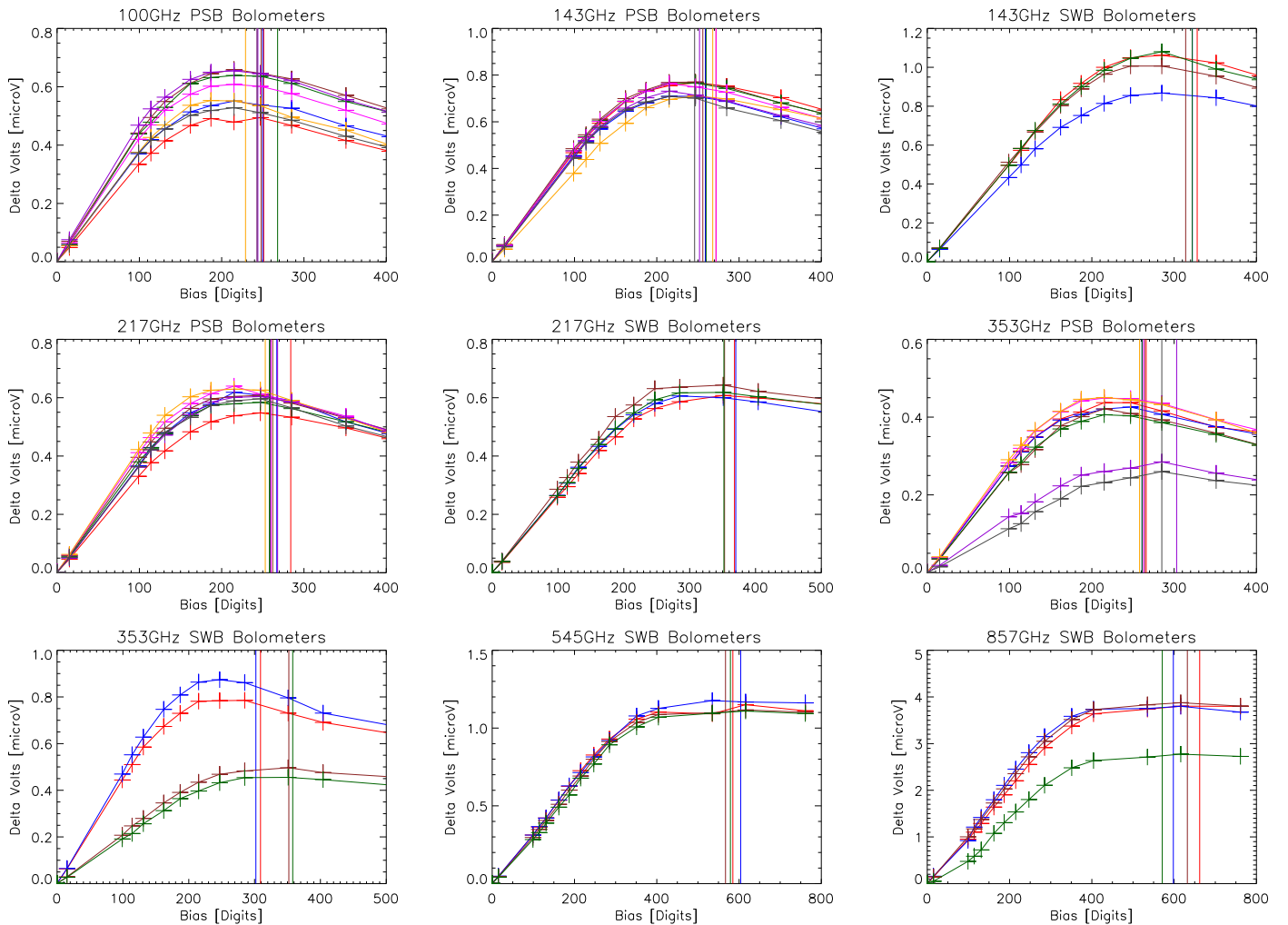


Figure 2. Optimization of the bolometer bias currents. Vertical lines indicate the final bias value setting. These values are shifted with respect to the maximum because a dynamic response correction has been taken into account. A bias value of 100 digits corresponds approximately to 0.1 nA.

et al. 2010; Pratt 1978). In flight, the value of σ was determined at the end of the CPV phase after subtraction of the signal from the timeline.

The two means $\langle S_{\text{REU}} \rangle$ and $\langle S_{\text{demod}} \rangle$ computed as 32-bit words are sent through the telemetry, together with the $S_{\text{DPU},i}$ values. A variable length encoding of the $S_{\text{DPU},i}$ values is performed on board, and the inverse decoding is applied on ground. This provides a lossless transmission of the quantized values. A load limitation mechanism inhibits the data transmission, first at the compression slice level (compression errors), and second at the ring level (Lamarre et al. 2010).

For a given Q value, the load on each channel depends on the dynamic range of the signal above the level of the noise. This dynamic range is largest for the high frequency bolometers because of the galactic signal. The large rate of glitches due to high energy particle interactions also contributes to the load of each channel. Optimal use of the bandpass available for the downlink (75 kb s^{-1} average for HFI science) was obtained by using initially a value of $Q = \sigma/2.5$ for all bolometer signals, therefore including a margin with respect to the requirement of $\sigma/Q = 2$. The load on each HFI channel is shown and compared to simulated data in Fig. 3. The increase of signal gradients

while scanning through the galactic center in September 2009 triggered the load limitation mechanism (compression error) and up to 80000 samples were lost for each of the 857 GHz band bolometers. Therefore a new value of $Q = \sigma/2$ was set for those bolometers from 21 December 2009 onward, reducing the number of samples lost to less than 200 during the following scan through the galactic center in March 2010. An illustration of a compression error loss is shown in Fig. 4. Thanks to the redundancy of the *Planck* scan strategy and the irregular distribution of the few remaining compression errors, no pixels are missing in the maps of the high signal-to-noise ratio galactic center regions. Periodic checks of the noise value σ are done for each channel, but no deviation requiring a change in the quantization step Q has been encountered so far.

3.2.5. Instrument readiness at the end of the CPV phase

The overall readiness of the instrument was assessed during the FLS. This end-to-end test was completely successful, from both the instrument setting and the satellite scanning points of view. The part of the sky covered during the FLS was included in the first all sky survey.

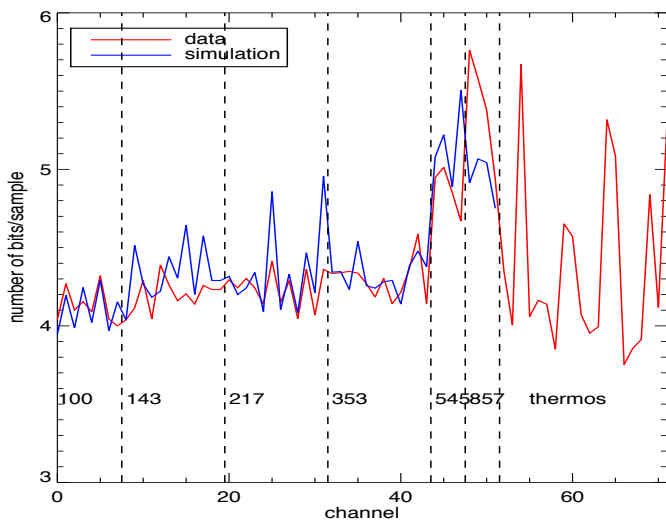


Figure 3. Load measured for each HFI channel on 16 July 2010. Simulated data for the same patch of the sky are shown for bolometers. Channels #54 and higher correspond to the fine thermometers on the optical stages of the instruments, plus a fixed resistor (#60) and a capacitor (#61) on the bolometer plate.

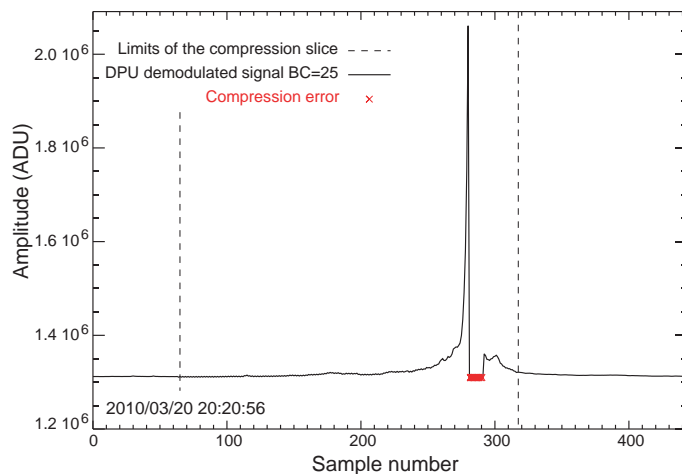


Figure 4. Example of loss in one compression slice of data on bolometer 857-1. Note the large signal-to-noise ratio while scanning through the galactic center.

3.3. Response

3.3.1. Variation of the signal with background and with the bolometer plate temperature

The optical background on the bolometers originates from the sky, the telescope, and from the HFI itself. The operating point of the bolometers is constrained by this total optical background, and the fluctuations of this background have a direct impact on the stability of the HFI measurements.

The power spectral density of each contribution to the background is compared to 30% of the total noise measured in-flight (NEP₁ column of Table 6). This specification corresponds to a quadratic contribution smaller than 5% on the total noise.

The in-flight temperature stability of the HFI cryogenic

Table 3. Relative response deviation (in %) from linearity for the CMB dipole, the galactic center (GC) and planets. Saturation (Sat.) occurs for the Jupiter measurements at high frequency.

	Dipole	GC	Mars	Saturn	Jupiter
100 GHz	$3.8 \cdot 10^{-4}$	0.001	0.01	0.13	0.8
143 GHz	10^{-3}	0.0017	0.02	0.18	1.0
217 GHz	$8 \cdot 10^{-4}$	0.003	0.05	0.53	3.2
353 GHz	$6.4 \cdot 10^{-4}$	0.007	0.06	0.8	4.5
545 GHz	$< 10^{-4}$	0.01	0.08	0.8	Sat.
857 GHz	$< 10^{-4}$	0.1	0.06	0.8	Sat.

stages is discussed in [Planck Collaboration \(2011b\)](#). The optical coupling of the HFI bolometers to each cryogenic stage is shown in the left panels of Figs. 5 and 6 and in Fig. 7. (The fact that the 100 mK couplings all agree with pre-launch measurements shows that no bolometers were damaged during launch.) These couplings are used to calculate the effect of the fluctuations of each cryogenic stage on the bolometer signals. The right panels of Figs. 5 and 6 show the power spectral density (PSD) of the respective thermometers scaled by the optical coupling factors for the most extreme bolometers. The scaled PSDs of the thermal fluctuations of the 4 K and 1.4 K stages are below the line corresponding to 30% of the total noise of the corresponding bolometer for all frequencies above the spacecraft spin frequency.

The bolometer plate thermometers have a large cosmic particle hit rate ([Planck Collaboration 2011b](#)) because of the large size of their sensors compared to that of the bolometers. Cosmic ray hits detection and removal do not allow us to reach the thermometer nominal sensitivity, therefore they cannot be used to remove the effect of bolometer plate temperature fluctuations on the bolometer signal. Instead, the data processing pipeline ([Planck HFI Core Team 2011b](#)) uses blind bolometers located on the bolometer plate. The bolometer noise components are discussed in Sect. 6.

3.3.2. Linearity

The way a bolometer transforms absorbed optical power into a voltage is not a linear process because both the conductance between the bolometer and the heat sink, and the bolometer impedance have a non-linear dependence on the temperature (see e.g. [Catalano \(2008\)](#); [Sudiwala et al. \(2000\)](#)).

The characterization of the linearity of the HFI detectors has a direct impact on the calibration of the instrument: strong non-linearity takes place during the galaxy crossing for high frequency bolometers and during planet crossings. An accurate absolute calibration is also necessary for the CMB dipole. Finally, the energy scale of large glitches can be corrected. The static response has been characterized during ground calibration showing a small deviation from linearity around a tenth of one percent for fainter sources (few hundreds of attowatts) and around a few percent for brighter sources like planets ([Pajot et al. 2010](#)). The static response measured during the CPV phase agrees with the ground estimate to better than 1%. Nevertheless, the use of the static non-linearity determination does not represent the true bolometric non-linear behaviour when

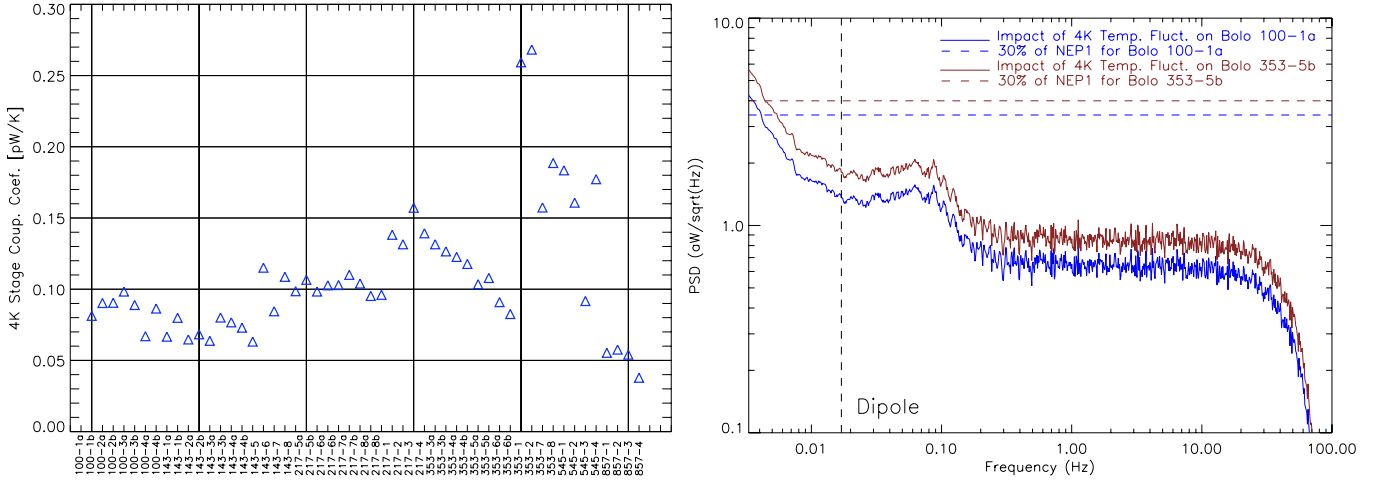


Figure 5. Left: coupling coefficients of the 4 K stage. Right: scaled power spectral density (PSD) of the 4 K stage thermal fluctuations for the 100-1a and 353-5a-7a bolometers.

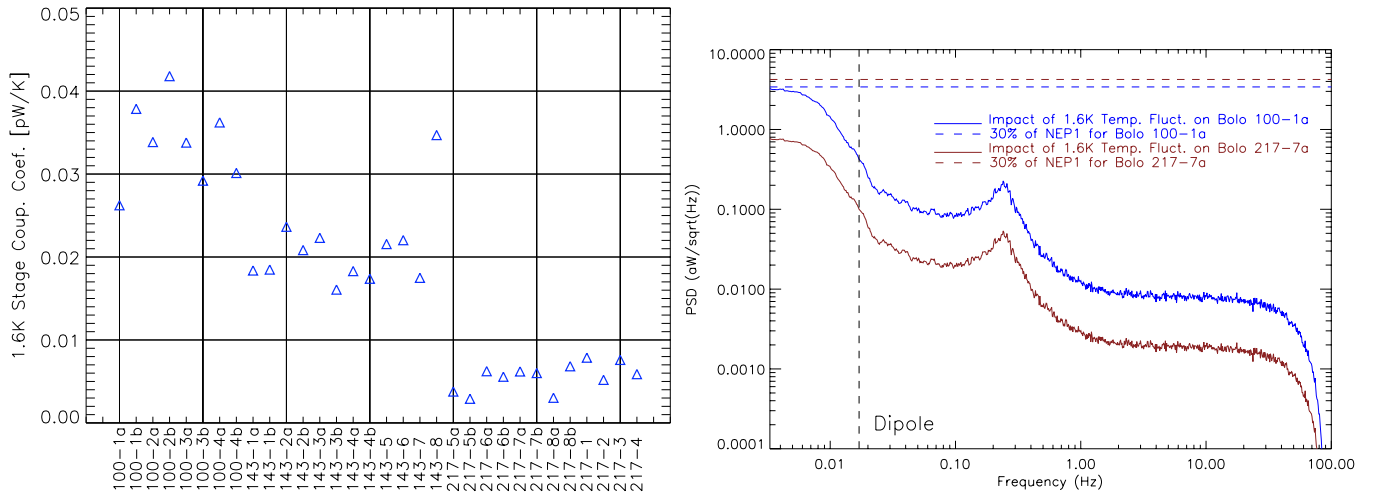


Figure 6. Left: coupling coefficients of the 1.4 K stage. The thermal emission in high frequency bands becomes too small to be measured. Right: scaled PSD of the 1.4 K stage thermal fluctuations for the 100-1a and 353-5a-7a bolometers.

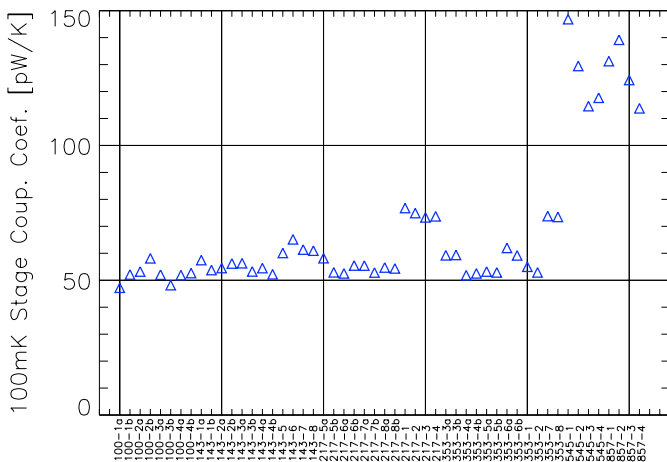


Figure 7. Bolometer signal coupling coefficients to the 100mK bolometer plate.

scanning through bright point sources like planets. The linearization of the response done by multiplying the signal

times the gain (depending on the amplitude of the signal) and convolving it with the temporal transfer function normalized to 1 at the lowest frequency, is valid in the case of small signals. However this is not the case for bright point sources for which the estimate of non-linearity using the static response may be incorrect by up to 40% in the extreme case of Jupiter. For these sources we use a model to correct the static results. The use of fainter planets like Mars to characterize the beams minimizes this effect.

Table 3 gives the deviation from linearity for various sources at the center of the beam for the bolometers at each frequency.

3.4. Electrical crosstalk on HFI detectors

The electrical coupling of the signal of one bolometer into the readout chain of another, or *electrical crosstalk*, was measured to be less than -60 dB for all pairs of channels during ground-based tests (Pajot et al. 2010). We performed two tests in flight to verify this result, described below.

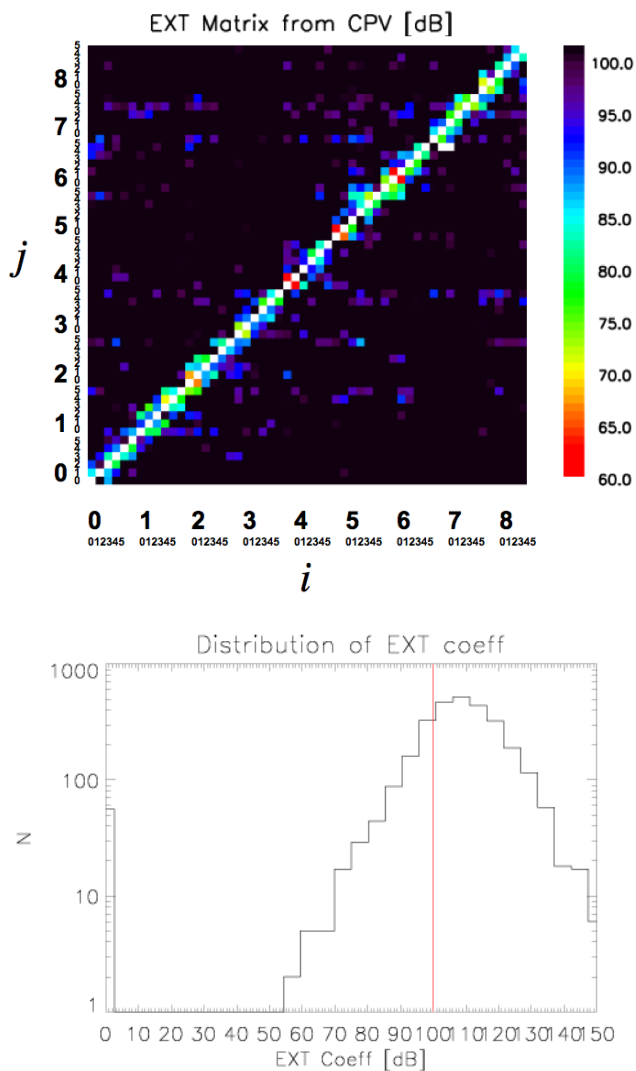


Figure 8. Top: Electrical crosstalk matrix C_{ij} 54x54 for all bolometers, coefficients are in dB. Bottom: Distribution of electrical crosstalk coefficients in dB.

3.4.1. CPV crosstalk measurements

During the CPV phase, we switched off each readout channel one at a time for ten minutes, and observed the impact on all other channels. For each bolometer we collected about 660 minutes of data.

The crosstalk coefficient between channels i and j is expressed as:

$$C_{ij} = \Delta \tilde{V}_j / \Delta \tilde{V}_i, \quad (3)$$

where \tilde{V}_i and \tilde{V}_j are the channel i and j voltages, corrected for thermal drift. The crosstalk matrix and a histogram of crosstalk levels are shown in Fig. 8. The crosstalk is mostly confined to nearest neighbours in the belt, channels whose wiring is physically close. The measured crosstalk level is in good agreement with ground measurements, typically < -70 dB, and thus meets the requirement. A few of the polarization sensitive bolometer pairs show a crosstalk around -60 dB.

In the next section we see that crosstalk measurement from glitches shows a much lower level of crosstalk. These

results suggest that the CPV test has measured electrical crosstalk in current which is unrelated to the scientific signal.

3.4.2. Measurements using glitches

We used high energy glitches in one channel to study the impact on the signal of surrounding channels. Thousands of glitch events are collected for one channel, and the signals of all other channels for the same time period are stacked. The crosstalk in volts for individual glitches is defined as:

$$c_{ij}^V = \Delta V_j / \Delta V_i \quad (4)$$

where V_i is the glitch amplitude in volts in the channel hit by a cosmic ray, and V_j the response amplitude of another channel j . Then, for a pair of channels i and j , the global voltage crosstalk coefficient is

$$C_{ij}^V = \text{median}(c_{ij}^V) \quad (5)$$

For SWB channels, in contrast with the CPV previous results, no evidence of crosstalk is seen, with an upper limit of -100 dB. There are outliers in galactic channels because of incorrect glitch flagging. A second analysis using planet crossing data instead of glitches gave the same results.

Concerning the coupling between PSB pairs, we see crosstalk around -60 dB, in agreement with the CPV tests; however, this is likely an upper limit because it includes the effects of coincident cosmic ray glitches which produce a similar effect but are not crosstalk.

4. Beams and time response

4.1. Measurement of Time Response

4.1.1. Introduction

The *time response* of HFI describes the shift, in amplitude and phase, between the optical signal incident to each detector and the output of the readout electronics. The response can be approximated by a linear complex transfer function in the frequency domain. The signal band of HFI extends from the spin frequency of the spacecraft ($f_{\text{spin}} \simeq 16.7$ mHz) to a cutoff defined by the angular size of the beam (14–70 Hz; see Table 4 from Lamarre et al. (2010)). For the channels at 100, 143, 217, and 353 GHz, the dipole calibration normalizes the time response at the spin frequency. To properly measure the sky signal at small scales, the time response must be characterized to high precision across the entire signal band, spanning four decades from 16.7 mHz to ~ 100 Hz.

The time response of bolometers typically is nearly flat over a signal band from zero frequency to a frequency defined by the bolometer's thermal time constant, and then drops sharply at higher frequencies. For the HFI bolometers, the thermal frequency is 20–50 Hz (Lamarre et al. 2010; Holmes et al. 2008), as noted in Lamarre et al. (2010) and Pajot et al. (2010), however, the time response of HFI is not flat at very low frequencies, but exhibits a low frequency excess response (LFER).

We define the *optical beam* as the instantaneous directional response to a point source. Any sky signal is convolved with this function, which is completely determined by the optical systems of HFI and *Planck*.

Since *Planck* is rotating at a nearly constant rate and around the same direction, the data are the convolution of the signal with both the beam and the time response of HFI. We separate the two effects and deconvolve the time response from the time ordered data. This deconvolution results in a flat signal response, but necessarily amplifies any components of the system noise that are not rolled off by the bolometric response. This amplified noise is suppressed by a low-pass filter (Planck HFI Core Team 2011b).

4.1.2. TF10 model

The main ingredients of the time response are: (i) heat propagation within the bolometer; (ii) signal modulation at a frequency of $f_{\text{mod}} = 90.188$ Hz performed by reversing the bolometer bias current; (iii) the effect of parasitic capacitance along the high impedance wiring between the bolometer and the first electronics stage (JFETs); (iv) band-pass filtering, to reject the low frequency and high frequency white noise in the electronics; (v) signal averaging and sampling; and (vi) demodulation.

Because of the complexity of this sequence, a phenomenological approach was chosen to build the time response model. The time response is written as the product of three factors:

$$H_{10}(f) = H_{\text{bolo}} \times H_{\text{res}} \times H_{\text{filter}} \quad (6)$$

Schematically, the first factor takes into account step (i), the second factor describes a resonance effect that results from the combination of steps (ii) and (iii), while the purpose of H_{filter} is to account for step (iv).

Detailed analysis and measurements of heat propagation within the bolometer have shown that H_{bolo} is given by the algebraic sum of three single pole low pass filters. Explicitly:

$$H_{\text{bolo}} = \sum_{i=1,3} \frac{a_i}{1 + j2\pi f \tau_i} \quad (7)$$

with 6 parameters ($a_1, a_2, a_3, \tau_1, \tau_2, \tau_3$).

$$H_{\text{res}} = \frac{1 + p_7(2\pi f)^2}{1 - p_8(2\pi f)^2 + jp_9(2\pi f)} \quad (8)$$

with 3 free parameters (p_7, p_8, p_9),

$$H_{\text{filter}} = \frac{1 - (f/F_{\text{mod}})^2}{1 - p_{10}(2\pi f)^2 + j(f/F_{\text{filter}})^2} \quad (9)$$

with one free parameter (p_{10}). A total of 10 free parameters describe this model, as indicated by its name. See Fig. 9 for an illustration of the three components of the time response model TF10 for a typical 217 GHz channel.

The parameter F_{filter} characterizes the rejection filter width and is kept fixed to 6 Hz in the fitting process. Besides the fact that this phenomenological model is physically motivated, this parameterization:

- ensures causality
- satisfies $H(-f) = H^*(f)$
- goes to 1 when f goes to zero (because we define $a_1 + a_2 + a_3 = 1$), while it goes to 0 when f goes to infinity
- includes enough parameters to provide the necessary flexibility to fit the time response data of all 52 bolometers.

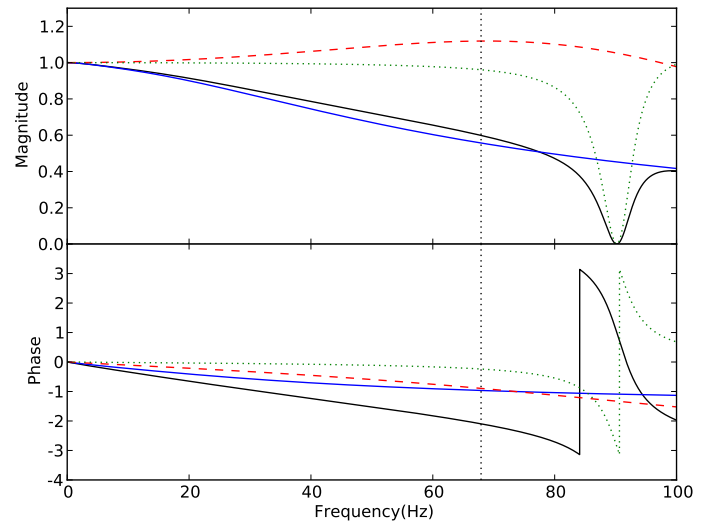


Figure 9. The amplitude and phase (in radians) of the three components of the TF10 model of the time response. The solid blue line is $H_{\text{bolo}}(f)$, the dotted green line shows $H_{\text{filter}}(f)$ and the dashed red line shows H_{res} . The solid black line is $H_{10}(f)$, the product of the three components. The vertical dotted black line shows the signal frequency where the beam of a 217 GHz channel cuts the signal power by half.

4.1.3. Fitting the TF10 Model to Ground Data

To obtain the 10×52 parameter values, we used three sets of pre-launch measurements. (i) The bolometer response was measured at 10 different frequencies by illuminating all 52 bolometers with a chopped light source. (ii) Other measurements were done using carbon fibers as light sources; the latter were alternately turned on and off at a variable frequency. (iii) The bolometer bias currents were periodically stepped up and lowered by a small amount. By adding a square wave to the DC current, temperature steps are induced, simulating turning on and off a light source (the analysis of these data requires bolometer modelling).

None of these measurements was absolutely normalized; all compared the relative response to inputs of various frequencies. While measurement (i) only provided the amplitude of the time response, measurements (ii) and (iii) provided both the amplitude and the phase. Note that for the phase analysis, because of the lack of precise knowledge of the time origin t_0 of the light/current pulses, a fourth factor $\exp(j2\pi\Delta t_0 f)$ is introduced in the expression of $H_{10}(f)$, where the additional parameter Δt_0 represents the uncertainty in time.

Among the three sets of measurements, the carbon fiber set covered the largest frequency range. Thus it was the best for building the transfer function model described above and for investigating its main features. However, it involves uncertainties that could be resolved only with a very detailed simulation of the set-up, therefore it was not used to calculate the final set of parameter values. The final values were calculated from data sets (i) and (iii), whose frequency ranges are complementary, 2–140 Hz and 0.0167–10 Hz, respectively. Since no absolute normalization was available, the two datasets were matched in the overlap frequency range.

The fitting of the analytic expression given above to the merged data was done in the range between 16.7 mHz and 120 Hz. The 52 fits have a χ^2/DoF distribution whose mean value is 1.13, indicating that the model is adequate to describe the data. The numerical values of p_{10} displayed a small spread, $\sigma_{\text{mean}} < 6 \times 10^{-4}$. This parameter was set at its mean value to calculate the 52 covariance matrices of the nine remaining parameters, which were useful in propagating the statistical errors.

As described below, the time response thus obtained was further tuned and checked using in-flight observations, in particular signals produced by planets and by cosmic rays (glitches).

An alternative model has also been defined, based on the analytical expression of the steps (ii) to (vi) of section 4.1.2. Based on a closer analysis of the electronics stages, this model is more physically motivated than the 10-parameter model. It requires only 8 parameters and provides better results near the modulation frequency. Nevertheless the model has not been used in the current data release. It is only used as a benchmark, to check possible systematic effects in the current release. Most of the effects of the difference between the models disappear when the data are low-pass filtered.

4.1.4. Fitting TF10 to Flight Data

The planets Mars, Jupiter, and Saturn are bright, compact sources that are suitable for measuring the beam and provide a near-delta-function stimulus to the system that can be used to constrain the time response. During the first sky survey, *Planck* observed Mars twice and Jupiter and Saturn once (Planck HFI Core Team 2011b). During a planet observation, the spacecraft scans in its usual observing mode (Planck Collaboration 2011a), shifting the spin axis in 2' steps along a cycloidal path on the sky. Since planets are close to the ecliptic plane, the coverage in the cross-scan direction is not as fine as in the scan direction. In the case of Jupiter and Saturn, each channel observes the planet once per rotation for a period of approximately 6 hours (9 periods of stationary pointing, or "rings"). Because Mars has a large proper motion, the first observation lasted 12 hours (or 18 rings).

We use the forward-sense time domain approach (Huffenberger et al. 2010) to simultaneously fit for Gaussian beam parameters and TF10 time response parameters. A custom processing pipeline avoids filtering the data. We extract the raw bolometer signal and demodulate it using the parity bit. We use the flags created by the time ordered information (TOI) processing pipeline to exclude data samples contaminated by cosmic rays, and we additionally flag all data samples where the nonlinear gain correction is more than 0.1%. We use Horizons² ephemerides to compute the pointing of each horn relative to the planet center.

The time domain signal from the planet is modeled as an elliptical Gaussian convolved with the TF10 time response as follows:

$$d(t) = H_{10} \star A(t)G[\mathbf{x}(t); \mathbf{x}_0, \epsilon, \theta_{FWHM}, \psi] \quad (10)$$

where the Gaussian optical beam model G is parameterized as in Eqs. 9–11 of Huffenberger et al. (2010), except the

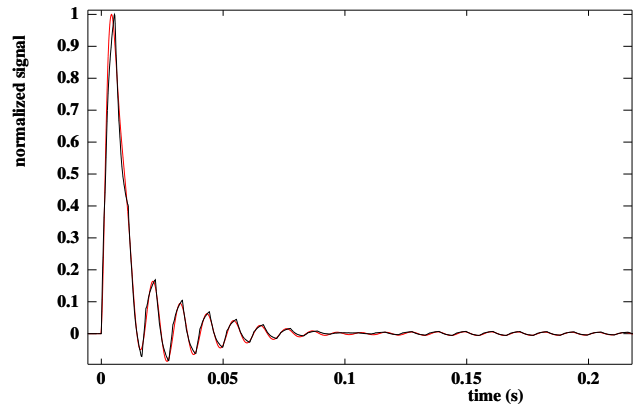


Figure 10. Comparison of the impulse response of channel 143-2a (red curve) and a template made from stacking glitch events (black curve). Noise begins to dominate further in the timeline. The ringing observed at the modulation frequency is generated by the electronics rejection filter.

planet amplitude is parameterized with a disk temperature rather than a single amplitude:

$$A(t) = T_{\text{disk}} \frac{\Omega_p(t)}{\Omega_b}, \quad (11)$$

where T_{disk} is the whole-disk temperature of the planet, Ω_p is the solid angle of the planet, which can vary significantly during the observation, and Ω_b is the solid angle of the beam. Ω_p is computed using Horizons, which is programmed with *Planck*'s orbit.

The free parameters of the fit are the six parameters of the time response corresponding to H_{bolo} , the two components of the centroid of the beam \mathbf{x}_0 , the mean FWHM θ_{FWHM} , the ellipticity ϵ , the ellipse orientation angle ψ , and the planetary disk temperature T_{disk} . The four parameters describing the electronics are somewhat degenerate with the bolometer part of the time response, and we fix them at the ground-based values.

Because of the large nonlinear response and highly non-Gaussian beams at 545 and 857 GHz, we do not perform fits to the planet data at these frequencies. Instead we rely on pre-launch fits for the time response.

By taking the Fourier transform of the time response function derived on planets, one obtains the system response to a Dirac impulse. This response can be compared to the glitches generated by cosmic rays that deposit energy in the sensor grids.

The glitches detected by HFI are sampled with time steps $1/(2F_{\text{mod}})$. However, the glitches can be superresolved in time by normalizing, phasing, and stacking single glitch events (Crill et al. 2003). This gives glitch templates for each channel (Alexandre Sauvé, private communication) that are effectively sampled at a much higher frequency.

Figure 10 shows the comparison between a superresolved glitch template and the corresponding calculated response. There is good agreement in general, but there are discrepancies at high frequency ($f > 100$ Hz). The physical model for the electronics transfer functions briefly described at the end of section 4.1.3 suppresses this discrepancy at high frequency.

² ssd.jpl.nasa.gov/?horizons

Each planet observation suffers unique systematic effects, so a comparison of the time response recovered on each gives a good assessment of the effects of these different systematics. Mars has a large proper motion, giving excellent sampling in the cross-scan direction; however, there is a known diurnal variability in its brightness temperature (Swinyard et al. 2010). Jupiter has a large angular diameter (48'') relative to the HFI beam size, and Saturn and Jupiter are so bright that the HFI detectors are driven significantly nonlinear (see Table 3). Nonetheless, we find that the time response is consistent to 0.1-0.5% when recovered from each of the planets individually as well as from all planets simultaneously.

A further cross-check is done by stacking planet scans to build a superresolved planet timeline. Time response parameters are fit to the superresolved planet using the assumption of a near-Gaussian beam profile, and are consistent with the first approach.

The in-flight time response differs from the ground-based time-response by at worst 1.5% between 1 Hz and 40 Hz. We do not include this difference in the final error budget, because it is likely that the time response has changed due to differences in background conditions.

4.1.5. Low Frequency Excess Response

The HFI bolometers show low frequency excess response (LFER), (Lamarre et al. 2010). Though the planets are bright, the short impulse they provide is close to a delta function and the energy is spread evenly across nearly all harmonic components. In combination with low frequency noise, the measurements are not sensitive to frequencies below ~ 0.5 Hz; so with planet observations alone we cannot constrain an excess response at very low frequency. We maintain the ground measurements as our best estimation of the LFER. In the ground-based measurements the bias step vs. carbon fiber differs by at most 1.5% at low frequency, so we assign a systematic error of 1.5% for frequencies below 0.5 Hz.

For future data releases, we will use the difference of sky signal between surveys to constrain the LFER.

4.1.6. Summary of Errors in the Time Response

As noted above, the data represent the combined effect of the time response and the optical beam. The time response, however, is not degenerate with a Gaussian parameterization of the beam; the true beams deviate from a Gaussian shape at the several percent level near the main lobe, while time response effects tend to give the beam an extended tail following the planet in the scan direction. The Gaussian assumption could slightly bias the recovered time response; however, any residual bias is captured in the measurement of the post-deconvolution scanning beam (Planck HFI Core Team 2011b).

Because of the high signal-to-noise ratio of the planet data, statistical errors in the fit are small, so we assess the systematic errors in the resulting time response by checking the consistency of various methods of recovering the time response. We fit to different combinations of planet data: Mars, Jupiter, and Saturn data separately and all of the data simultaneously to check for systematics resulting from various planets. Additionally we compare the planet-fitted

time response with ground-based data and with the impulse response from cosmic ray glitches.

Our final error budget is as follows:

- Low frequency ($f < 0.5$ Hz): the errors are dominated by the possibility of a low frequency excess response below 0.5 Hz at a level of 1.5%.
- Middle frequency ($0.5 \text{ Hz} < f < 50 \text{ Hz}$): We set an error bar between 0.1% and 0.5% depending on the channel. This error bar is set by the consistency in results from different sets of planet data.
- High frequency: ($f > 50 \text{ Hz}$) Our empirical model of the electronics in the TF10 model does not describe the system very well at these frequencies, as shown by some disagreement between the glitches and the TF10 impulse response. However, for this data release, the low-pass filter applied to the data and the beam cutoff reduce the importance of this frequency band.

The *Planck* scan strategy is such that the same region of the sky is observed scanning in nearly opposite directions six months apart. An error in the time response is highlighted in the difference of maps obtained from the first six months and the second six months of the survey. This difference map shows some level of contamination, in particular near the Galactic plane, where the signal is higher. The same level of contamination is observed in simulations in which the data are generated with a transfer function, and analysed with a different one, in order to mimic the uncertainties described above. With this technique, we validate the error budget.

4.2. Optical Beams

The *optical beam* is defined (Sect. 4.1.1) as the instantaneous directional response to a point source. For HFI, the optical beams for each channel are determined by the telescope, the horn antennas in the focal plane and, for the polarized channels, by the orientations of their respective polarization sensitive bolometers (PSBs) (Maffei et al. 2010). Model calculations of the beams are essential, since it was possible to measure only a limited number of beams in the telescope far-field before launch. The 545 and 857 GHz channels, which employ multimoded corrugated horns and waveguides, were not included in this campaign. (The optical beam is related to, but is not the same as the *scanning beam* defined in Planck HFI Core Team (2011b) and used for data analysis purposes.) Tauber et al. (2010b) reported the best pre-launch expectations for the optical beams, obtained using physical optics calculations with CORRUG³ and GRASP⁴. Table 4 compares the calculated and measured (Sect. 4.1.2) beams for the single-moded channels (up to 353 GHz).

For these channels the pre-launch calculations of FWHM and ellipticity and measured Mars values agree to within a few percent. These differences are contained within 2.7σ of the data errors. The main source of discrepancy could be a slight misalignment of the pre-launch telescope model with respect to the actual in-flight telescope geometry, which is currently being investigated (Jensen & et al 2010).

³ SMT Consultancies Ltd. www.smtconsultancies.co.uk

⁴ TICRA, www.ticra.com

Table 4. Comparison of pre-launch calculations and measured parameters for the HFI optical beams (band averages). Standard deviations σ are computed as the dispersion between the Saturn, Jupiter, and Mars data for each given channel.

Band	Expected FWHM [']	Mars FWHM [']	Mars σ_{FWHM} [']	Expected ellipticity	Mars ellipticity	Mars σ_{ellip}
100P	9.58	9.37	0.06	1.17	1.18	0.006
143P	6.93	6.97	0.10	1.06	1.02	0.004
143	7.11	7.24	0.10	1.03	1.04	0.005
217P	4.63	4.70	0.06	1.12	1.13	0.006
217	4.62	4.63	0.06	1.10	1.15	0.010
353P	4.52	4.41	0.06	1.08	1.07	0.009
353	4.59	4.48	0.04	1.23	1.14	0.007
545	4.09	3.80	–	1.03	1.25	–
857	3.93	3.67	–	1.04	1.03	–

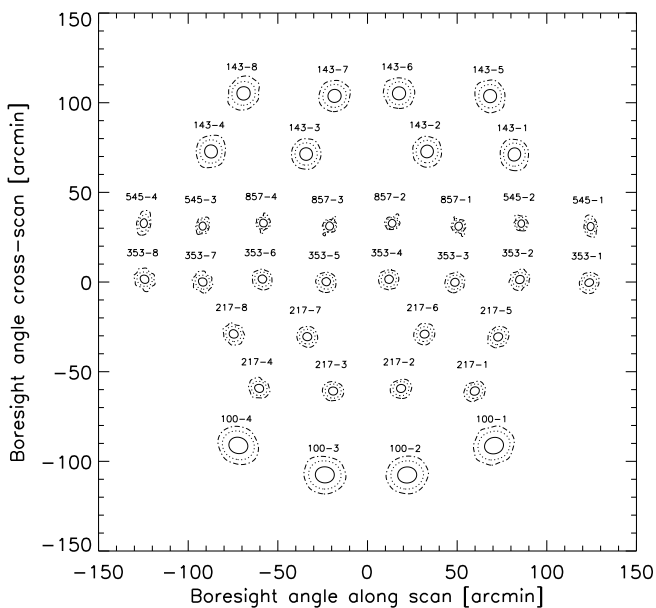


Figure 11. The distribution of the HFI beams on the sky relative to the telescope boresight as viewed from infinity. Contours of the Gauss-Hermite decomposition of the Mars data at 1%, 10%, and 50% power levels from the peak. For the photometers containing a pair of PSBs, the average beam of the two PSBs is shown.

Table 5 reports our best knowledge of the FWHM of the optical beams for each channel. We stress that this table does not provide parameters of the scanning beam of the processed data, which accounts for the additional effects of the instrument time response and of the time domain filtering in the data processing (Planck HFI Core Team 2011b).

As reported in Maffei et al. (2010), the 545 GHz and 857 GHz channels are multimoded (more than one electromagnetic mode propagating through the horn antennas) and their optical beams are markedly non-Gaussian. The understanding of these channels through simulations has progressed since *Planck* was launched, especially in the characterization of their modal content (Murphy et al. 2010).

In Table 4 we compare pre-launch calculations of the beams with the beams measured with Mars. Differences in FWHM are less than 7%. We stress that this discrepancy does not impact the scientific products of the *Planck* mis-

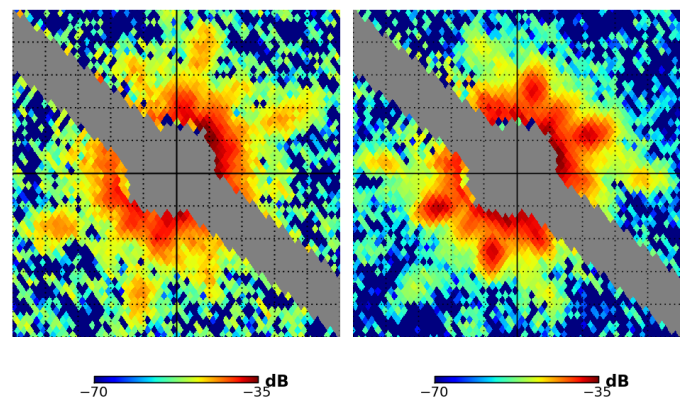


Figure 12. The “dimpling effect” as seen at 545 GHz (left panel) and 857 GHz (right panel). The grid spacing is $10'$. The color scale is in dB normalized to the peak signal of Jupiter.

sion since the scanning beams are the ones to be used for data analysis purposes. From an instrumental point of view, the inflight measurements must obviously be considered as the reference for the performance of these channels.

The development of the HFI multimoded channels necessitated the novel extension of previously existing modelling techniques for the analysis of the corrugated horn antennas and waveguides, as well as for the propagation of partially coherent fields (modes) through the telescope onto the sky (Murphy et al. 2001). Extensive pre-launch measurement campaigns were conducted for all the HFI horn antenna/filter assemblies (Ade et al. 2010). The HFI multimoded channels are suitable for the scientific goals of *Planck*. Nevertheless, for future instruments, more research can be envisaged in this field. The characterization of the modal filtering in the horn-waveguide assembly and the understanding of the coupling of the waveguide modes to the detector need further theoretical and experimental study.

The similarity of the pre-launch expectations to our current knowledge of the HFI focal plane (beams and their positions on the sky) tells us that the overall structural integrity of the focal plane has been preserved after launch. Furthermore, the optical beams as measured on Mars are shown in Fig. 11 and can be compared with the equivalent representations of the focal plane layout based on calcu-

Table 5. Geometric mean of the asymmetric gaussian FWHM.

Bolometer	beam FWHM	spectral Band cut-on	spectral Band cut-off
Name	[\prime]	GHz	GHz
100-1a	9.46	84.9	113.87
100-1b	9.60	87.0	115.27
100-2a	9.41	86.5	116.28
100-2b	9.43	84.4	115.42
100-3a	9.42	84.4	116.77
100-3b	9.47	84.4	116.77
100-4a	9.43	84.9	117.79
100-4b	9.45	84.9	117.79
143-1a	6.91	120.8	161.77
143-1b	6.99	120.3	162.78
143-2a	6.78	119.8	162.26
143-2b	6.80	119.3	163.28
143-3a	6.91	120.3	158.73
143-3b	6.86	120.3	160.75
143-4a	7.01	118.8	167.83
143-4b	7.01	119.3	161.26
143-5	7.45	120.3	166.31
143-6	7.08	120.3	165.81
143-7	7.18	120.8	167.83
143-8	7.20	120.8	165.3
217-5a	4.73	184.0	249.72
217-5b	4.75	183.9	249.12
217-6a	4.66	182.5	253.26
217-6b	4.64	189.6	252.76
217-7a	4.63	188.6	253.77
217-7b	4.68	189.6	250.74
217-8a	4.69	182.5	253.26
217-8b	4.73	182.0	252.76
217-1	4.68	189.6	249.72
217-2	4.61	189.1	253.26
217-3	4.59	191.1	252.76
217-4	4.61	193.1	252.76
353-3a	4.47	310.9	403.91
353-3b	4.46	310.4	405.93
353-4a	4.40	323.5	400.88
353-4b	4.39	313.9	406.94
353-5a	4.41	302.3	405.43
353-5b	4.42	299.8	405.93
353-6a	4.47	300.3	406.94
353-6b	4.45	314.4	397.84
353-1	4.57	310.4	401.38
353-2	4.46	312.9	407.45
353-7	4.44	326.1	404.4
353-8	4.53	318.5	405.92
545-1	3.94	466.1	638.93
545-2	3.63	464.5	633.87
545-3	3.79	467.6	633.87
545-4	4.17	479.2	635.89
857-1	3.73	748.1	986.59
857-2	3.66	736.5	982.65
857-3	3.76	747.1	984.21
857-4	3.67	744.1	970.02

lations in earlier papers (Maffei et al. 2010; Tauber et al. 2010b). A detailed account of the full focal plane reconstruction can be found in Planck HFI Core Team (2011b).

There is a “dimpling” of the reflector surfaces from the irregular print-through of the honeycomb support structures on the reflector surfaces themselves (Tauber et al. 2010b). GRASP calculations predict that this will generate a series of rings of narrow bright grating lobes around the main lobe. Since the small-scale details of the dimpling

structure of the *Planck* reflectors are irregular, these grating lobes tend to merge with the overall power scattered by the reflector surfaces (Ruze scattering (Ruze 1966)). Fig. 12 shows a HEALPIX (Górski et al. 2005) map of the first survey observation of Jupiter minus the second survey observation of the same sky region to remove the sky background. We see the first ring of grating lobes as expected in the map from all 545 and 857 GHz channels, where the signal-to-noise ratio on the planets is highest. The inner 15' of the beam is saturated and does not appear in the map. At 857 GHz, the discrete grating lobes appear at level below -35 dB with respect to the peak (~ 30 dB), and represent a negligible fraction of the total beam throughput. The shoulder of the beam, extending radially to $\sim 15'$, represents a larger contribution to the throughput, ranging from 0.5% to a few percent for the CMB and sub-mm channels, respectively.

5. Noise properties

The *Planck* HFI is the first example of space-based bolometers, continuously cooled to 100 mK for several years. Although the detectors were thoroughly tested on the ground (Lamarre et al. 2010; Pajot et al. 2010), it remained then to be seen how they would behave in the L2 space environment. We describe here the noise properties of the HFI in the first year of operation, focusing on the differences between space and ground performance.

This section deals with the Gaussian part of the noise. Section (6) describes the systematic effects that have been analyzed in the data so far.

An example of raw time ordered information (TOI) is shown in Fig. 13. The TOI is dominated by the signal from the CMB dipole, Galactic emission, point sources, and glitches. Therefore, the noise properties cannot be directly deduced from the TOI. We first describe the general method used to evaluate the noise, then we give general statements on the noise properties.

5.1. Noise estimation

The Level-2 *detnoise* pipeline (Planck HFI Core Team 2011b) is used to determine a noise power spectrum, from which one extracts the noise equivalent power (NEP) of the detectors (see Planck HFI Core Team (2011b) for a full description). The pipeline uses redundancies in the observations to determine an estimate of the sky signal, which is then subtracted from the full TOI to produce a pure noise timeline. The signal estimates are the integration of typically 40 circles of data at a constant spin axis pointing. The average signal, binned in spin phase, provides an accurate estimate of the signal. This signal as a function of spin phase is then subtracted from the TOI. The residual is an estimate of the instantaneous noise. Power spectra of this residual timeline are then obtained for each pointing period (see Fig. 14) and fit for the white noise level, i.e., the NEP, in the spectral region between 0.6 and 2.5 Hz. The lower limit of 0.6 Hz is high enough that the low frequency excess noise can be neglected and the upper limit small enough to keep the time response near to its value at low frequencies (16 mHz) at which the instrument is calibrated.

The noise is stable at a level better than 10% in the majority of detectors. Exceptions are: (1) a few rings

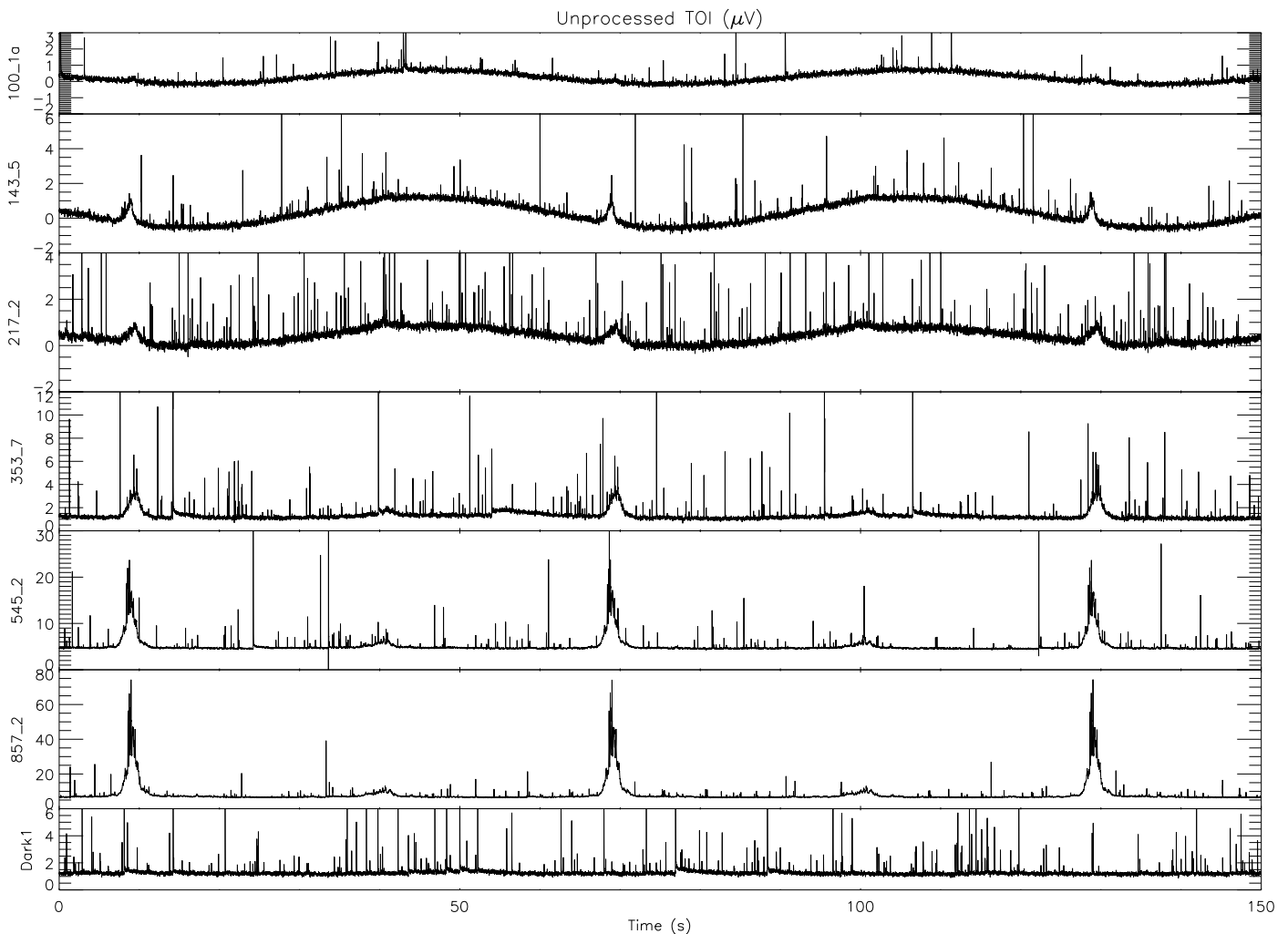


Figure 13. Examples of raw (unprocessed) TOI for one bolometer at each of six HFI frequencies and one dark bolometer. Slightly more than two scan circles are shown. The TOI is dominated by the CMB dipole, the Galactic dust emission, point sources, and glitches. The relative part of glitches is over represented on these plots due to the thickness of the lines that is larger than the real glitch duration.

with unusual events that contaminate the measurement, e.g., poorly corrected/flagged glitches or passage over very strong sources such as the Galactic centre, especially at 857 GHz; (2) a weak trend, smaller than 1% in amplitude, that correlates with the duration of the pointing period (an expected bias due to the ring average signal removal); (3) bolometers affected by random telegraph signals (RTS) (see next Section); and (4) some uncorrelated jumps in the noise levels for about ten bolometers at the 30% level for isolated periods of a few days. The overall result is that a very clear *baseline* value can be identified and can be used to determine the NEP of each bolometer. This is then converted to $NE\Delta T$ with the help of the flux calibration. The $NE\Delta T$ s thus measured are given in Table 6. The quoted uncertainties are derived from the rms of the NEPs in a band around the baseline.

5.2. The noise components

The detector noise is described by the combination of several components:

- Photon and bolometer noise, which appear as white

noise filtered by the time response of the bolometer, the readout electronics, and the TOI processing.

- Electronics and Johnson noise, which produce noise that is nearly white across the frequency band, but with a sharp decrease at the high frequency end due to the on-board data handling and the TOI filtering.
- The 4K lines (Sect 6), appearing as residuals in the spectra.
- The energy deposited by cosmic rays on the bolometers, which appears as "glitches", i.e., positive peaks in the signal, which are removed by the TOI processing (Sect. 6, and [Planck HFI Core Team \(2011b\)](#)). Residuals from glitches appear in the noise spectrum as a bump between 0.1 and 1 Hz.
- Low frequency excess (LFE) noise, which is present below about 100 mHz.

The last three sources of noise are detailed in Section 6.

There is additional noise (of the order of 0.5% or less) due to the on-board quantization of the data before transmission. In general, the noise level, as measured by the NEP, is between 10 and 20 $\text{aW Hz}^{-1/2}$ for the 100 to 353 GHz channels, and between 20 and 40 $\text{aW Hz}^{-1/2}$ for

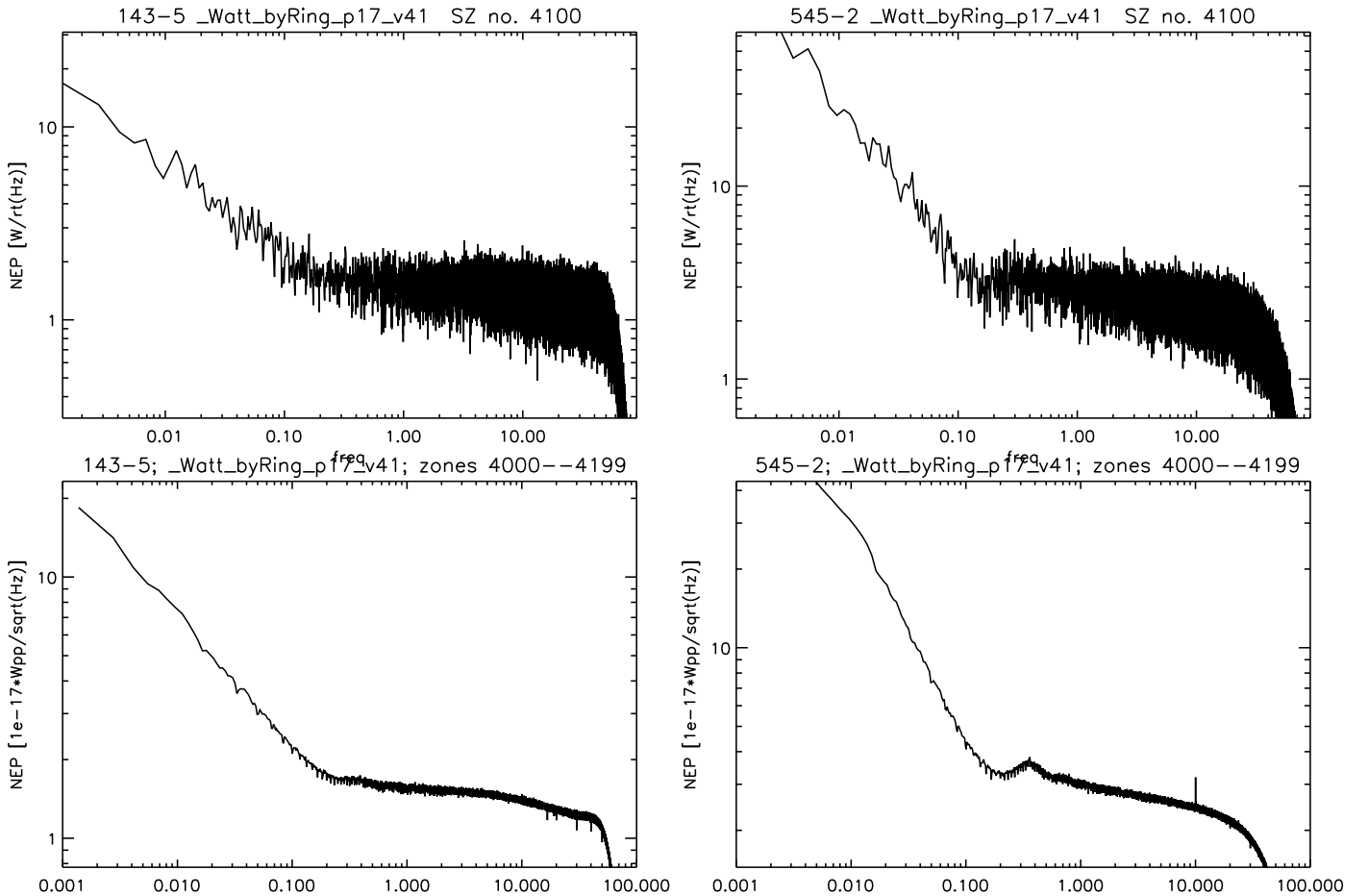


Figure 14. Typical power spectrum amplitude of bolometers 143-5 and 545-2. For the upper panels, this is the power spectrum density of valid samples, after an average ring (the sky signal) has been subtracted from the TOI. Stacking of the result for 200 rings is shown in the lower panel. Here, the instrument time response is not deconvolved from the data.

the 545 and 857 GHz channels. It is in line with the ground-based expectations and the lower estimate of the background load with a detector-to-detector variability of less than 20% (see Sect. 8).

Due to the AC bias modulation scheme, the $1/f$ noise from the electronics is aliased near the modulation frequency where it is heavily filtered out. The benefit of this scheme is visible on the noise power spectrum of the 10 M Ω resistor which shows a flat spectrum at the Johnson value down to 1 mHz, a tribute to the electronic chain stability.

At the present time, we assume that the LFE noise, not observed in ground-based measurements, is mostly due to the 100 mK bolometer plate fluctuations. While drifts in the 100 mK stage that are correlated between bolometers are removed, there are likely local temperature fluctuations due to particle energy deposited close to each detector.

6. First assessment of systematic effects

6.1. 4K lines

The fundamental frequency of the ^4He -JT cooler (40.083373 Hz) is phase-locked to the frequency of the data acquisition (180.37518 Hz) in a ratio of 2 to 9. EMI/EMC impacts the TOI only as very narrow lines. Unfortunately, in flight, unlike in ground-based measurements, these lines are not stable. The 4K line variations are illustrated in

Fig. 15. The variability of the lines is in part due to temperature fluctuations in the service module of the *Planck* spacecraft. Indeed, some of the variability was related to the power cycling of the data transponder which, for stability reasons, has been kept on continuously since 25 January 2010 (OD 258, [Planck Collaboration 2011b](#), see Fig. 16).

6.2. Abnormal noise in the electronics

Of the 54 bolometers on HFI, three show a significant RTS, also known as “popcorn noise.” These are 143-8, 545-3, and 857-4. Fig 17 illustrates their behaviour. The noise timeline clearly exhibits a two-level system. The three RTS bolometers in flight are the ones where RTS occurred most frequently in ground measurements. However, in flight: 1) the level difference is well above the noise (at least ten times the rms); 2) the two-level system can be a three-level system or even larger; and 3) the RTS is intermittent. For large duration, it can be unnoticeable, especially for the 857-4 bolometer.

In an unrelated fashion, we see uncorrelated jumps in the noise TOI of many bolometers at a rate of just a few every year.

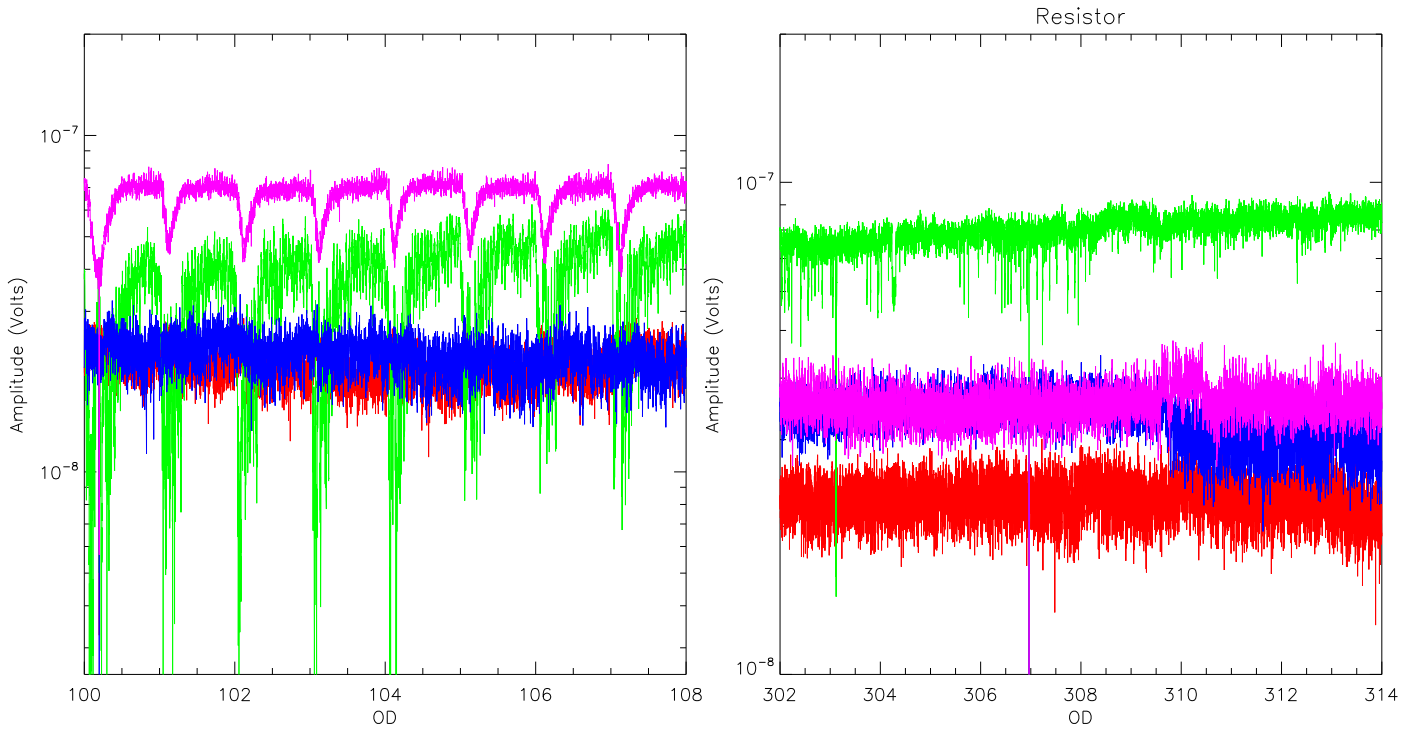


Figure 16. Zoom on the four main 4 K line systematics amplitude measured in the TOI processing on the test resistance. (*Left*) Period when the transponder was switched on once per day for the 3-hours Daily Tele-Communication Period (DTCP). (*Right*) Period when the transponder was kept on at all times, later in the mission.

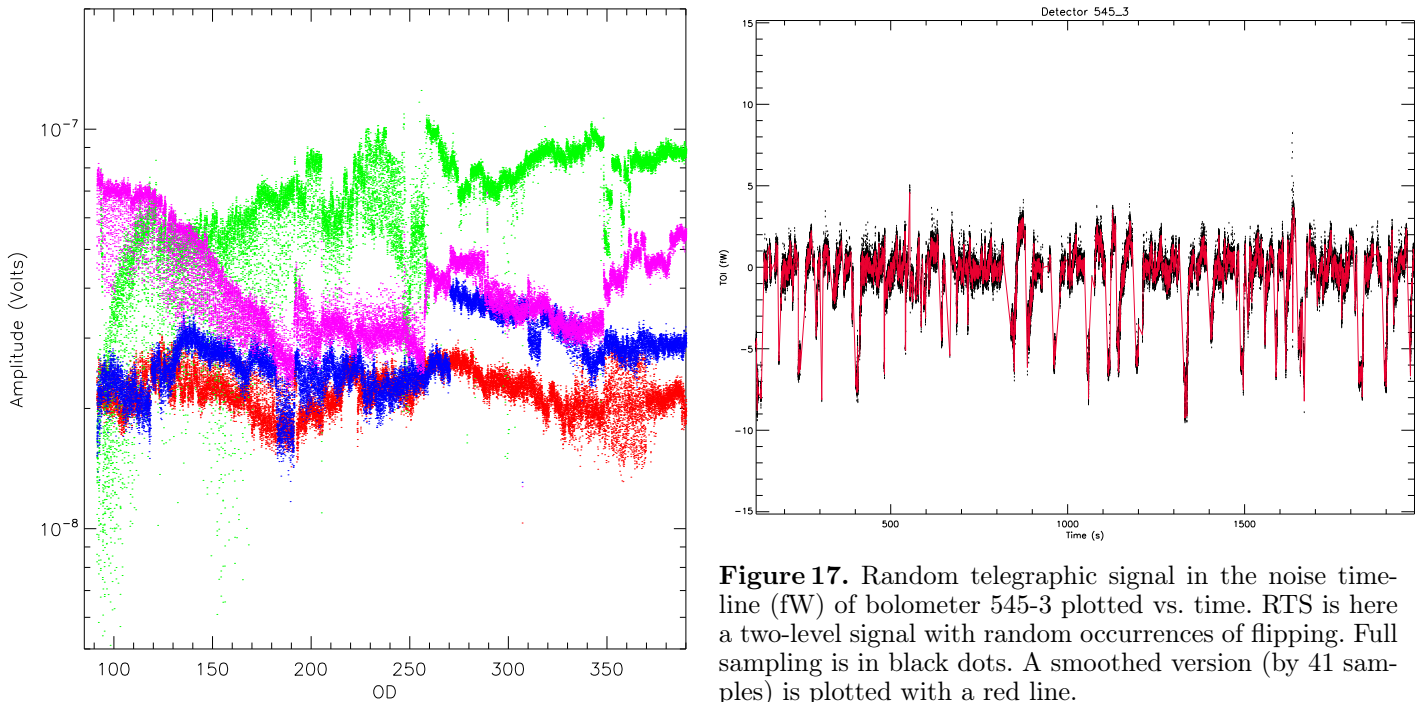


Figure 15. Typical trend of the cosine and sine coefficient variation of the four main 4 K lines measured in the TOI processing on the test resistance at 10, 30, 50, and 70 Hz

Figure 17. Random telegraphic signal in the noise timeline (fW) of bolometer 545-3 plotted vs. time. RTS is here a two-level signal with random occurrences of flipping. Full sampling is in black dots. A smoothed version (by 41 samples) is plotted with a red line.

6.3. Cosmic rays and their effects

Energy is deposited by cosmic rays in various parts of the HFI instrument. We observe these events in the TOIs of all detectors as a signal peak characterised by a very short

rise time (less than 1.5 ms) and an exponential decay. These events are called glitches. The other effect of the cosmic rays is a thermal input to the bolometer plate, which induces low frequency noise on the bolometers. Thermal effects are described in [Planck HFI Core Team \(2011b\)](#) and their very long term consequences detailed in Sect. 7.

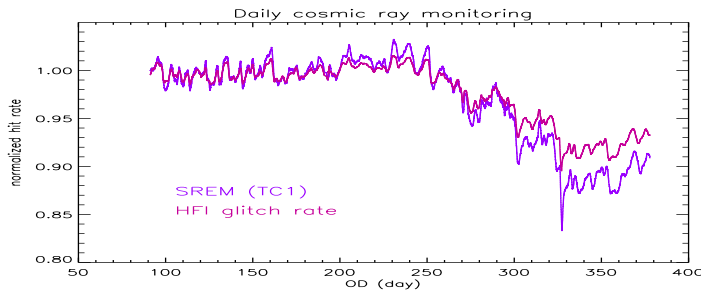


Figure 18. SREM hit count and HFI bolometer average glitch rate evolution. SREM TC1 hit counts measure the protons with a deposited energy larger than 0.085 MeV.

6.4. Cosmic ray-induced glitch spectrum seen by *Planck*

Cosmic rays consist of two main components at the L2 location of *Planck*: the Solar component and the Galactic component. The Solar component is at low energy (a few keV) except during flares, when energies can reach GeV. HFI is immune to the low energy component and no major flares have yet been recorded. The Galactic component (Shikaze et al. 2007) with a maximum between roughly 300 MeV and 1 GeV, is modulated by Solar activity. The *Planck* mission began during the weakest solar activity for a century (McDonald et al. 2010). Hence, the Galactic cosmic ray component is expected to be at its highest level.

The glitch rate evolution (Fig. 18) follows closely the proton monitoring by the space radiation environment monitor (SREM), a piggy-back experiment mounted on the *Planck* spacecraft. This figure shows that cosmic rays are the main source of HFI glitches. The glitch rate tended to decrease during the mission since January 2010 due to the slow increase of the Solar activity.

This glitch rate can be understood as the sum of two interaction modes, depending on whether the cosmic ray has a direct or indirect interaction with the bolometer. High energy cosmic rays can also interact with the bolometer plate and induce thermal effects and correlated glitches on the bolometers. These are dealt with in Sect. 7. The glitch characteristics also depend on the location of the energy deposit within the bolometer: the thermistor, the absorbing grid, or the bolometer housing.

6.4.1. Direct interaction

Cosmic ray particles can deposit energy directly on the thermistor or the absorbing grid. This is observed at well-defined deposited energies corresponding to the thickness of the element. Typically thermistor hits are about 20 keV, whereas grid hits are about 2 keV. These events occur at a rate of a few per minute.

6.4.2. Indirect interaction

Cosmic ray particles can also deposit energy indirectly. All particles crossing some matter produce a shower of secondary electrons, through ionization, that are mostly absorbed in the matter nearby. However, interactions occurring within microns of the internal surface of the bolometer box produce a shower of free secondary particles. A fraction of these particles is absorbed by the thermistor and the grid of the bolometer. This explains the large coincidence

rate of glitches between PSB bolometers *a* and *b* sharing the same mounting structure. The energy of those glitches follows a power law distribution spanning the whole range, from the detection threshold to the saturation level. This spectrum is expected for the delta and secondary electrons produced via the ionization process. The total rate of these events is typically one per second, and thus dominates the total counts shown in Fig. 19.

A more detailed description of the effect of cosmic rays on HFI detectors is postponed to a dedicated paper, and glitch handling in the data processing is described by Planck HFI Core Team (2011b).

7. Instrument stability

The radiative power reaching each bolometer is the co-addition of the flux from the sky and of the thermal emission of all optical elements "seen" from the detector: filters, horns, telescope reflectors, shields, and mechanical parts visible in the side-lobes. In addition, fluctuations of the heat sink temperature (the bolometer plate) appear like an optical signal. Any change in any of the parameters (temperature, emissivity, geometrical coefficient) driving these sources may be visible in the bolometer signal as a "DC level", i.e. a stable or very slowly varying (days) component in the signal.

Monitoring the "DC level" supposes that one is able to remove the varying sky signal from the stable sources. This is done in the map-making process (Planck HFI Core Team 2011b) by using the redundancy of the scanning strategy. Fig. 20 shows for the 217 GHz bolometers the history of the DC level during nearly one year. All follow a pattern similar to that of the cosmic ray activity measured by the SREM (see Sect. 6 and Fig. 18), which indicates that cosmic rays are at the origin of the measured signal. One can check on families of bolometers with non-uniform heat leaks *G* that this signal is directly related to temperature variations of the bolometer plate and not to external optical sources. In fact, we can see here residual fluctuations that the PID of the bolometer plate fails to compensate because its efficiency is far from one. The similarity of Fig. 20 and Fig. 18, also shows that the effect of gain variations and of DC level drifts of the readout electronics is small with respect to other sources of signal drifts.

It should be noted that the "DC level" variation of 217 GHz bolometers is equivalent to an optical power of a couple of femtowatts, while the total background power on these bolometers is about 1 pW. This fluctuation is mainly due to the energy deposited by cosmic rays on the bolometer plate, which means that the "equivalent power" of the other sources of temperature fluctuation and of optical background fluctuations are no more than a fraction of femtowatt, i.e. less than one part per thousand of the background.

The change of gain induced by the DC level variations can be estimated from the non-linearity measurements (see Sect. 3.3.2). In the case considered in Fig. 20, the relative gain change is of the order of a few 10^{-4} .

During the CPV phase, the readout electronics was "balanced", i.e. the offset parameter was tuned to get a signal near to zero. During the first year of operation, and for all bolometers, deviations from this point remained small with respect to the total range of acceptable values. In consequence, no re-tuning of the readout electronics was

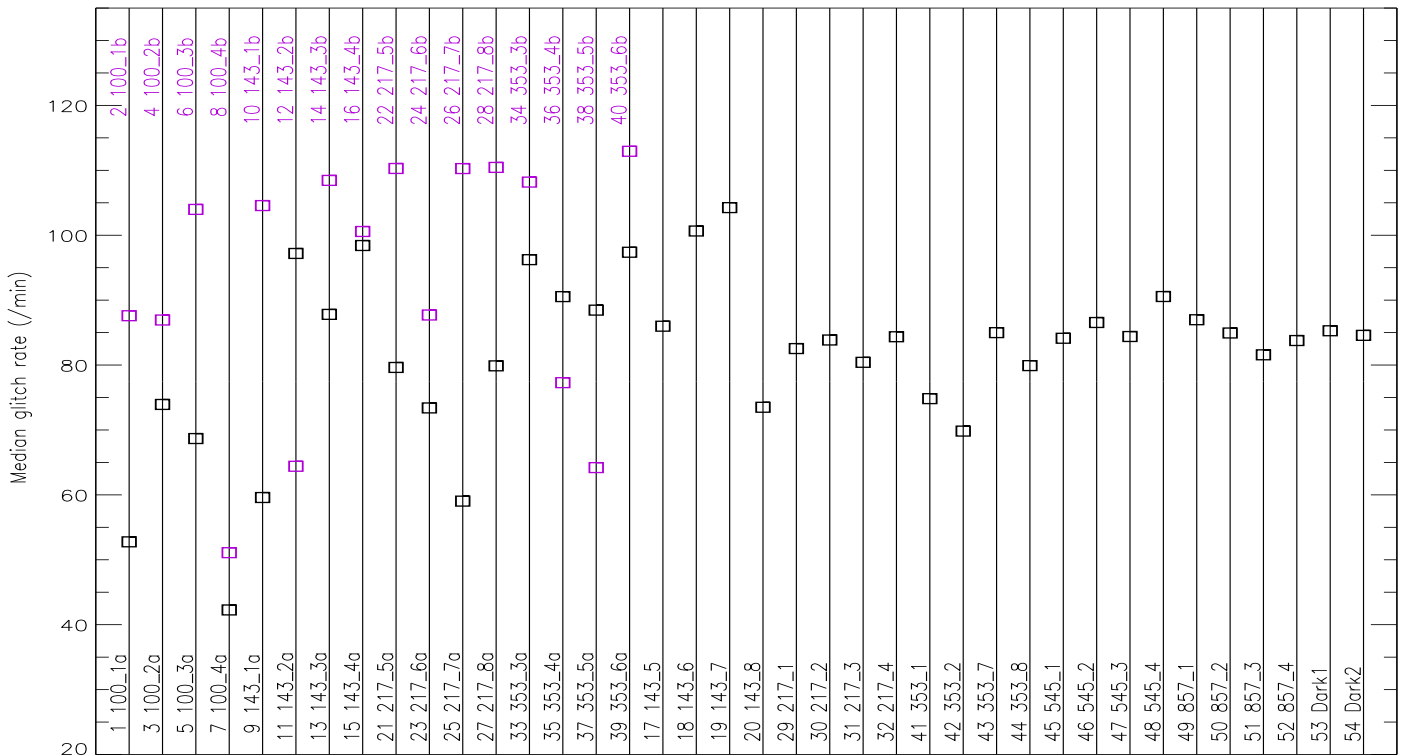


Figure 19. Glitch rate of all HFI bolometers. An average over the first sky survey has been performed. The asymmetry between PSB bolometers sharing the same horn is an effect of detection threshold and asymmetric time constant properties between PSB *a* and *b*.

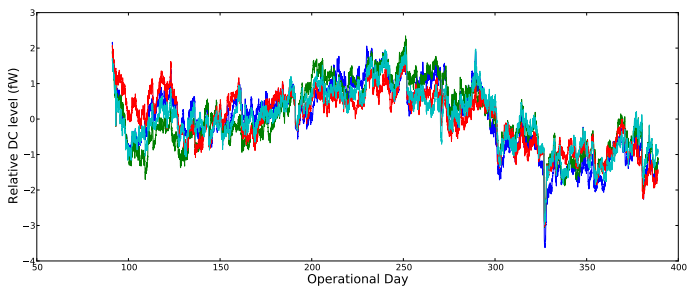


Figure 20. The drift in the DC level of the 217 GHz SWB bolometers, in femtoWatts of equivalent power in the detector, for the first year of operation.

needed during this period and it is expected to be the same up to the end of the mission.

8. Main performance parameters

The primary difference between the in-flight and pre-launch performance of the HFI derives from the relatively high rate of cosmic rays in the L2 environment. At the energies of interest, the low level of solar activity results in an elevated cosmic ray flux. The glitches that result from cosmic ray events must be identified and removed from the time ordered information prior to processing the data into maps. The TOI processing also removes a significant fraction of the common mode component that appears in the bolometer TOIs at low frequencies. A residual low-frequency component is removed during the map-making process (Planck HFI Core Team 2011b).

Table 6 summarizes the noise properties of the processed TOI (Planck HFI Core Team 2011b), by the following parameters:

- A white noise model. NEP_1 is the average of the Noise Equivalent Power spectrum in the 0.6–2.5 Hz range.
- A model with a white noise NEP_2 plus a low frequency component: $NEP = NEP_2 [1 + (f_{knee}/f)^\alpha]$
- The sensitivity $NE\Delta T_{CMB}$ to temperature differences of the CMB. Note that this quantity is not particularly relevant for the channels at 545 and 857 GHz for which it takes large values that are highly dependent on the details of the spectral transmission for each detector.
- The sensitivity $NE\Delta T_{RJ}$ to temperature differences for sources observed in the Rayleigh-Jeans regime.

Figure 21 compares the goal, pre-launch and in-flight $NE\Delta T$ s. The average in-flight $NE\Delta T$ s are 27% higher than the pre-launch $NE\Delta T$ s. While the pre-launch and in-flight values are not directly comparable due to differences in the processing, these differences can account for less than half of the observed variation. The remaining part is attributed to residual contamination from cosmic rays that are not completely removed in the current TOI processing.

The sensitivity goals are taken from Table 1 of Lamarre et al. (2010), and are consistent with Table 1.3 of Planck Collaboration (2005) corrected for the use of PSBs at 100 GHz. Note that Fig. 21 supersedes Figure 11 of Lamarre et al. (2010) in which requirements and goals were improperly plotted. The in-flight sensitivities estimated from NEP_1 exceed the goals, which are defined by a total noise level equal to twice the expected contribution of photon noise. The average measured NEP_1 is typically 70% of the initial goal. The improvement in the NEP over the design

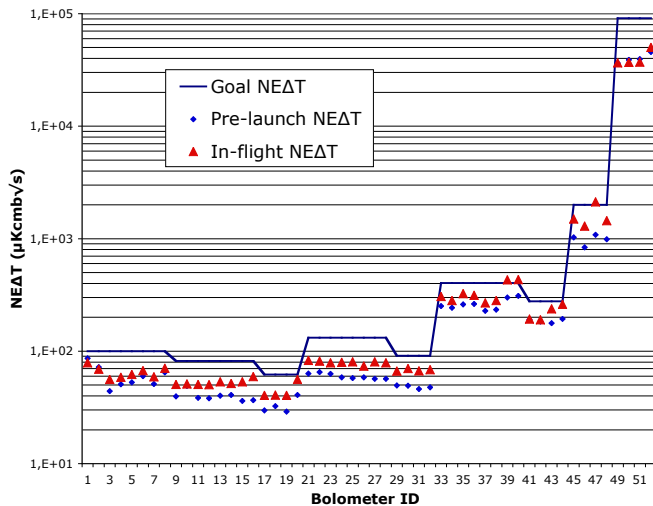


Figure 21. Noise Equivalent Delta Temperature measured on the ground and in-flight with slightly different tools

goals is primarily the result of having reduced the photon background through careful design of the optical system.

9. Conclusions

We report on the in-flight performance of the High Frequency Instrument on board the *Planck* satellite. These results are derived from the data obtained during a dedicated period of diagnostic testing prior to the initiation of the scientific survey, as well as an analysis of the survey data that form the basis of the early release scientific products.

With the exception of a single anomaly in the operation of the ^4He -JT cooler, the HFI has operated nominally since launch. The settings of the readout electronics determined during pre-launch testing were found to be very near the optimal value in flight and were applied without any modification. A random telegraphic signal is observed in the same three channels that exhibited this behaviour during the final pre-launch testing. These channels are currently excluded from the scientific analysis. The instrument operation has been extremely stable during the first year of operation, requiring no adjustment of the readout electronics.

The optical design, and the alignment of the optical assembly, relied on both theoretical analysis and testing at the subsystem level. The beams of the 545 and 857 GHz channels, which employ multimoded corrugated horns and waveguide, could not be measured on the ground. The actual beam widths of these channels measured on planets are in general smaller than the design goals and estimated values. The optical properties of the single mode channels are in excellent agreement with the design expectations.

A higher than expected cosmic ray flux, related to the level of Solar activity, results in a manageable loss of signal and degradation of thermal stability. Discrete cosmic ray events result in glitches in the scientific signal that are flagged and removed by an algorithm making use of the signal redundancy in the timeline. In addition to these single events, the cosmic ray flux contributes a significant thermal load on the sub-kelvin stage. Variations in this flux produce low-frequency fluctuations in the bolometer

plate that induce a common mode component to the scientific signal and the focal plane thermometry. Although a component correlated with the dark bolometer outputs is removed during the TOI processing, a residual low frequency contribution is removed at the map-making stage. With the exception of the three detectors affected by telegraph noise, the sensitivity measured above 0.6 Hz exceeds the design goals of all HFI channels. After the removal of the residual low frequency noise, the final sensitivity of the frequency maps exceeds the mission requirements, and approaches the goals, as described in the companion paper [Planck HFI Core Team \(2011b\)](#).

Acknowledgements. The *Planck* HFI instrument (<http://hfi.planck.fr/>) was designed and built by an international consortium of laboratories, universities and institutes, with important contributions from the industry, under the leadership of the PI institute, IAS at Orsay, France. It was funded in particular by CNES, CNRS, NASA, STFC and ASI. The authors extend their gratitude to the numerous engineers and scientists, who have contributed to the design, development, construction or evaluation of the HFI instrument. A description of the *Planck* Collaboration and a list of its members, indicating which technical or scientific activities they have been involved in, can be found at www.rssd.esa.int/index.php?project=PLANCK&page=Planck_Collaboration.

References

- Ade, P. A. R., Savini, G., Sudiwala, R., et al. 2010, *A&A*, 520, A11+
- Benoît, A., Ade, P., Amblard, A., et al. 2003a, *A&A*, 399, L25
- Benoît, A., Ade, P., Amblard, A., et al. 2003b, *A&A*, 399, L19
- Benoît, A., Sirbi, A., Bradshaw, T., et al. 1997, in *ESA Special Publication*, Vol. 400, Sixth European Symposium on Space Environmental Control Systems, ed. T.-D. Guyenne, 497–+
- Bersanelli, M., Mandolesi, N., Butler, R. C., et al. 2010, *A&A*, 520, A4+
- Bhandari, P., Bowman, R. C., Chave, R. G., et al. 2000, *Astrophysical Letters Communications*, 37, 227
- Bhandari, P., Prina, M., Bowman, R. C., et al. 2004, *Cryogenics*, 44, 395
- Bock, J. J., Chen, D., Mauskopf, P. D., & Lange, A. E. 1995, *Space Science Reviews*, 74, 229
- Bradshaw, T. W. & Orłowska, A. H. 1997, in *ESA Special Publication*, Vol. 400, Sixth European Symposium on Space Environmental Control Systems, ed. T.-D. Guyenne, 465–+
- Catalano, A. 2008, PhD thesis, École doctorale Astronomie et Astrophysique d’Île de France
- Catalano, A., Coulais, A., & Lamarre, J. 2010, *Appl. Opt.*, 49, 5938
- Church, S. E., Philhour, B. J., Lange, A. E., et al. 1996, in *ESA Special Publication*, Vol. 388, Submillimetre and Far-Infrared Space Instrumentation, ed. E. J. Rolfe & G. Pilbratt, 77–+
- Crill, B. P., Ade, P. A. R., Artusa, D. R., et al. 2003, *ApJS*, 148, 527
- Gaertner, S., Benoît, A., Lamarre, J.-M., et al. 1997, *A&AS*, 126, 151
- Górski, K. M., Hivon, E., Banday, A. J., et al. 2005, *ApJ*, 622, 759
- Holmes, W. A., Bock, J. J., Crill, B. P., et al. 2008, *Appl. Opt.*, 47, 5996
- Huffenberger, K. M., Crill, B. P., Lange, A. E., Górski, K. M., & Lawrence, C. R. 2010, *A&A*, 510, A58+
- Jensen, F. & et al. 2010, *Proceedings of the Fourth European Conference on Antennas and Propagation (EUCAP)*
- Jones, W. C., Ade, P. A. R., Bock, J. J., et al. 2006, *ApJ*, 647, 823
- Jones, W. C., Bhatia, R., Bock, J. J., & Lange, A. E. 2003, in *Presented at the Society of Photo-Optical Instrumentation Engineers (SPIE) Conference*, Vol. 4855, *Society of Photo-Optical Instrumentation Engineers (SPIE) Conference Series*, ed. T. G. Phillips & J. Zmuidzinas, 227–238
- Lamarre, J., Puget, J., Ade, P. A. R., et al. 2010, *A&A*, 520, A9+
- Leahy, J. P., Bersanelli, M., D’Arcangelo, O., et al. 2010, *A&A*, 520, A8+
- Maffei, B., Noviello, F., Murphy, J. A., et al. 2010, *A&A*, 520, A12+
- Mandolesi, N., Bersanelli, M., Butler, R. C., et al. 2010, *A&A*, 520, A3+
- McDonald, F. B., Webber, W. R., & Reames, D. V. 2010, *Geophys. Res. Lett.*, 37, 18101

Table 6. NEP₁ is the average of the NEP of processed signal in the band 0.6–2.5 Hz. NEP₂ is the white noise component of the NEP (see text). The NEΔTs are derived from the NEP₂. † is for the bolometers suffering from RTS.

Bolometer		Noise	Two component fit			CMB	RJ
Name	ID#	NEP ₁	NEP ₂	f _{knee}	α	NEΔT _{CMB}	NEΔT _{RJ}
		10 ⁻¹⁷ W/√Hz	10 ⁻¹⁷ W/√Hz	mHz		μK _{CMB} √s	μK _{CMB} √s
100-1a	1	1.13	1.04	218	0.93	78	60.7
100-1b	2	1.21	1.14	166	1.02	69	53.0
100-2a	3	1.22	1.16	126	0.96	56	42.9
100-2b	4	1.31	1.22	182	0.95	58	44.7
100-3a	5	1.22	1.16	117	1.01	61	47.4
100-3b	6	1.09	1.01	173	1.02	66	51.4
100-4a	7	1.23	1.18	109	0.97	59	45.2
100-4b	8	1.18	1.08	212	0.95	70	53.6
143-1a	9	1.35	1.31	91	1.11	50	30.4
143-1b	10	1.18	1.09	197	1.01	51	30.6
143-2a	11	1.28	1.20	161	0.97	50	30.3
143-2b	12	1.30	1.27	106	1.18	50	30.1
143-3a	13	1.35	1.26	202	1.01	53	32.2
143-3b	14	1.18	1.09	190	1.02	51	30.9
143-4a	15	1.27	1.18	185	0.99	53	31.7
143-4b	16	1.32	1.24	161	1.07	59	35.5
143-5	17	1.53	1.46	138	1.10	40	23.9
143-6	18	1.37	1.25	230	1.03	40	24.1
143-7	19	1.49	1.40	154	1.09	40	23.8
†143-8	20	2.2	1.60	1244	0.90	55	33.1
217-5a	21	1.35	1.30	117	1.10	82	26.4
217-5b	22	1.33	1.22	219	1.06	81	25.9
217-6a	23	1.30	1.25	107	1.07	78	25.1
217-6b	24	1.31	1.26	118	1.08	79	25.2
217-7a	25	1.41	1.36	98	1.07	80	25.4
217-7b	26	1.25	1.17	157	1.05	73	23.4
217-8a	27	1.37	1.31	148	1.05	80	25.5
217-8b	28	1.27	1.17	206	1.03	78	24.9
217-1	29	1.59	1.49	187	1.14	66	20.7
217-2	30	1.61	1.48	229	1.10	69	21.7
217-3	31	1.63	1.54	165	1.12	66	20.8
217-4	32	1.62	1.53	173	1.14	68	21.3
353-3a	33	1.53	1.43	174	0.98	305	21.9
353-3b	34	1.39	1.31	162	1.06	282	20.3
353-4a	35	1.34	1.28	124	1.04	324	22.6
353-4b	36	1.30	1.25	127	1.12	313	21.8
353-5a	37	1.26	1.21	121	1.05	268	19.4
353-5b	38	1.33	1.27	125	1.09	281	20.3
353-6a	39	1.47	1.38	208	1.08	429	30.7
353-6b	40	1.33	1.26	179	1.20	432	32.4
353-1	41	1.59	1.52	100	1.04	192	13.7
353-2	42	1.72	1.66	98	1.07	189	13.4
353-7	43	1.62	1.54	155	1.18	237	16.4
353-8	44	1.67	1.59	159	1.15	260	17.6
545-1	45	3.50	3.19	295	1.20	1490	8.7
545-2	46	2.93	2.66	322	1.20	1293	7.9
†545-3	47	4.48	3.70	431	1.23	2116	12.7
545-4	48	2.76	2.51	297	1.19	1446	8.7
857-1	49	3.59	3.31	222	1.20	36566	3.4
857-2	50	4.10	3.75	265	1.15	36923	3.8
857-3	51	3.47	3.21	236	1.20	37037	3.5
†857-4	52	3.64	3.00	622	1.09	50180	5.4
Dark1	53	1.17	1.14	136	1.42	16496	–
Dark2	54	1.39	1.35	148	1.40	19462	–

Mennella et al. 2011, *Planck* early results 03: First assessment of the Low Frequency Instrument in-flight performance (Submitted to A&A)

Montroy, T. E., Ade, P. A. R., Bock, J. J., et al. 2006, *ApJ*, 647, 813

Murphy, J. A., Colgan, R., Gleeson, E., et al. 2002, in *American Institute of Physics Conference Series*, Vol. 616, *Experimental Cosmology at Millimetre Wavelengths*, ed. M. de Petris & M. Gervasi, 282–289

Murphy, J. A., Colgan, R., O’Sullivan, C., Maffei, B., & Ade, P. 2001, *Infrared Physics and Technology*, 42, 515

Murphy, J. A., Peacocke, T., Maffei, B., et al. 2010, *Journal of Instrumentation*, 5, 4001

Pajot, F., Ade, P. A. R., Beney, J., et al. 2010, *A&A*, 520, A10+

Piactini, F., Ade, P. A. R., Bock, J. J., et al. 2006, *ApJ*, 647, 833

Planck Collaboration. 2005, ESA publication ESA-SCI(2005)/01

- Planck Collaboration. 2011a, *Planck* early results 01: The *Planck* mission (Submitted to A&A)
- Planck Collaboration. 2011b, *Planck* early results 02: The thermal performance of *Planck* (Submitted to A&A)
- Planck Collaboration. 2011c, *Planck* early results 07: The Early Release Compact Source Catalogue (Submitted to A&A)
- Planck Collaboration. 2011d, *Planck* early results 08: The all-sky early Sunyaev-Zeldovich cluster sample (Submitted to A&A)
- Planck Collaboration. 2011e, *Planck* early results 09: XMM-Newton follow-up for validation of *Planck* cluster candidates (Submitted to A&A)
- Planck Collaboration. 2011f, *Planck* early results 10: Statistical analysis of Sunyaev-Zeldovich scaling relations for X-ray galaxy clusters (Submitted to A&A)
- Planck Collaboration. 2011g, *Planck* early results 11: Calibration of the local galaxy cluster Sunyaev-Zeldovich scaling relations (Submitted to A&A)
- Planck Collaboration. 2011h, *Planck* early results 12: Cluster Sunyaev-Zeldovich optical Scaling relations (Submitted to A&A)
- Planck Collaboration. 2011i, *Planck* early results 13: Statistical properties of extragalactic radio sources in the *Planck* Early Release Compact Source Catalogue (Submitted to A&A)
- Planck Collaboration. 2011j, *Planck* early results 14: Early Release Compact Source Catalogue validation and extreme radio sources (Submitted to A&A)
- Planck Collaboration. 2011k, *Planck* early results 15: Spectral energy distributions and radio continuum spectra of northern extragalactic radio sources (Submitted to A&A)
- Planck Collaboration. 2011l, *Planck* early results 16: The *Planck* view of nearby galaxies (Submitted to A&A)
- Planck Collaboration. 2011m, *Planck* early results 17: Origin of the submillimetre excess dust emission in the Magellanic Clouds (Submitted to A&A)
- Planck Collaboration. 2011n, *Planck* early results 18: The power spectrum of cosmic infrared background anisotropies (Submitted to A&A)
- Planck Collaboration. 2011o, *Planck* early results 19: All-sky temperature and dust optical depth from *Planck* and IRAS — constraints on the “dark gas” in our Galaxy (Submitted to A&A)
- Planck Collaboration. 2011p, *Planck* early results 20: New light on anomalous microwave emission from spinning dust grains (Submitted to A&A)
- Planck Collaboration. 2011q, *Planck* early results 21: Properties of the interstellar medium in the Galactic plane (Submitted to A&A)
- Planck Collaboration. 2011r, *Planck* early results 22: The submillimetre properties of a sample of Galactic cold clumps (Submitted to A&A)
- Planck Collaboration. 2011s, *Planck* early results 23: The Galactic cold core population revealed by the first all-sky survey (Submitted to A&A)
- Planck Collaboration. 2011t, *Planck* early results 24: Dust in the diffuse interstellar medium and the Galactic halo (Submitted to A&A)
- Planck Collaboration. 2011u, *Planck* early results 25: Thermal dust in nearby molecular clouds (Submitted to A&A)
- Planck Collaboration. 2011v, The Explanatory Supplement to the *Planck* Early Release Compact Source Catalogue (ESA)
- Planck HFI Core Team. 2011a, *Planck* early results 04: First assessment of the High Frequency Instrument in-flight performance (Submitted to A&A)
- Planck HFI Core Team. 2011b, *Planck* early results 06: The High Frequency Instrument data processing (Submitted to A&A)
- Pratt, W. K. 1978, Digital image processing, ed. Pratt, W. K.
- Rosset, C., Tristram, M., Ponthieu, N., et al. 2010, A&A, 520, A13+
- Ruze, J. 1966, Proceedings of the IEEE, 54, 633
- Shikaze, Y., Haino, S., Abe, K., et al. 2007, Astroparticle Physics, 28, 154
- Sudwala, R. V., Maffei, B., Griffin, M. J., et al. 2000, Nuclear Instruments and Methods in Physics Research A, 444, 408
- Swinyard, B. M., Hartogh, P., Sidher, S., et al. 2010, A&A, 518, L151+
- Tauber, J. A., Mandolesi, N., Puget, J., et al. 2010a, A&A, 520, A1+
- Tauber, J. A., Norgaard-Nielsen, H. U., Ade, P. A. R., et al. 2010b, A&A, 520, A2+
- Zacchei et al. 2011, *Planck* early results 05: The Low Frequency Instrument data processing (Submitted to A&A)
- rue A. Domon et Léonie Duquet, Paris, France
- ² Atacama Large Millimeter/submillimeter Array, ALMA Santiago Central Offices Alonso de Cordova 3107, Vitacura, Casilla 763 0355, Santiago, Chile
- ³ CITA, University of Toronto, 60 St. George St., Toronto, ON M5S 3H8, Canada
- ⁴ CNES, 18 avenue Edouard Belin, 31401 Toulouse Cedex 9, France
- ⁵ CNRS, IRAP, 9 Av. colonel Roche, BP 44346, F-31028 Toulouse cedex 4, France
- ⁶ California Institute of Technology, Pasadena, California, U.S.A.
- ⁷ DAMTP, Centre for Mathematical Sciences, Wilberforce Road, Cambridge CB3 0WA, U.K.
- ⁸ DSM/Irfu/SPP, CEA-Saclay, F-91191 Gif-sur-Yvette Cedex, France
- ⁹ DTU Space, National Space Institute, Juliane Mariesvej 30, Copenhagen, Denmark
- ¹⁰ Department of Astronomy and Astrophysics, University of Toronto, 50 Saint George Street, Toronto, Ontario, Canada
- ¹¹ Department of Physics, Princeton University, Princeton, New Jersey, U.S.A.
- ¹² Department of Physics, University of California, One Shields Avenue, Davis, California, U.S.A.
- ¹³ Department of Physics, University of Illinois at Urbana-Champaign, 1110 West Green Street, Urbana, Illinois, U.S.A.
- ¹⁴ Dipartimento di Fisica, Università La Sapienza, P. le A. Moro 2, Roma, Italy
- ¹⁵ Dipartimento di Fisica, Università degli Studi di Milano, Via Celoria, 16, Milano, Italy
- ¹⁶ European Southern Observatory, ESO Vitacura, Alonso de Cordova 3107, Vitacura, Casilla 19001, Santiago, Chile
- ¹⁷ European Space Agency, ESTEC, Keplerlaan 1, 2201 AZ Noordwijk, The Netherlands
- ¹⁸ INAF - Osservatorio Astronomico di Trieste, Via G.B. Tiepolo 11, Trieste, Italy
- ¹⁹ INAF/IASF Bologna, Via Gobetti 101, Bologna, Italy
- ²⁰ INAF/IASF Milano, Via E. Bassini 15, Milano, Italy
- ²¹ INSU, Institut des sciences de l’univers, CNRS, 3, rue Michel-Ange, 75794 Paris Cedex 16, France
- ²² IPAG: Institut de Planétologie et d’Astrophysique de Grenoble, Université Joseph Fourier, Grenoble 1 / CNRS-INSU, UMR 5274, Grenoble, F-38041, France
- ²³ Imperial College London, Astrophysics group, Blackett Laboratory, Prince Consort Road, London, SW7 2AZ, U.K.
- ²⁴ Infrared Processing and Analysis Center, California Institute of Technology, Pasadena, CA 91125, U.S.A.

¹ Astroparticule et Cosmologie, CNRS (UMR7164), Université Denis Diderot Paris 7, Bâtiment Condorcet, 10

- ²⁵ Institut d'Astrophysique Spatiale, CNRS (UMR8617) Université Paris-Sud 11, Bâtiment 121, Orsay, France
- ²⁶ Institut d'Astrophysique de Paris, CNRS UMR7095, Université Pierre & Marie Curie, 98 bis boulevard Arago, Paris, France
- ²⁷ Institut de Ciències de l'Espai, CSIC/IIEEC, Facultat de Ciències, Campus UAB, Torre C5 par-2, Bellaterra 08193, Spain
- ²⁸ Institut de Radioastronomie Millimétrique (IRAM), Avenida Divina Pastora 7, Local 20, 18012 Granada, Spain
- ²⁹ Institut de Radioastronomie Millimétrique (IRAM), Domaine Universitaire de Grenoble, 300 rue de la Piscine, 38406, Grenoble, France
- ³⁰ Instituto de Astrofísica de Canarias, C/Vía Láctea s/n, La Laguna, Tenerife, Spain
- ³¹ Jet Propulsion Laboratory, California Institute of Technology, 4800 Oak Grove Drive, Pasadena, California, U.S.A.
- ³² Jodrell Bank Centre for Astrophysics, Alan Turing Building, School of Physics and Astronomy, The University of Manchester, Oxford Road, Manchester, M13 9PL, U.K.
- ³³ Kavli Institute for Cosmology Cambridge, Madingley Road, Cambridge, CB3 0HA, U.K.
- ³⁴ LERMA, CNRS, Observatoire de Paris, 61 Avenue de l'Observatoire, Paris, France
- ³⁵ Laboratoire AIM, IRFU/Service d'Astrophysique - CEA/DSM - CNRS - Université Paris Diderot, Bât. 709, CEA-Saclay, F-91191 Gif-sur-Yvette Cedex, France
- ³⁶ Laboratoire Traitement et Communication de l'Information, CNRS (UMR 5141) and Télécom ParisTech, 46 rue Barrault F-75634 Paris Cedex 13, France
- ³⁷ Laboratoire d'Astrophysique de Marseille, 38 rue Frédéric Joliot-Curie, 13388, Marseille Cedex 13, France
- ³⁸ Laboratoire de Physique Subatomique et de Cosmologie, CNRS, Université Joseph Fourier Grenoble I, 53 rue des Martyrs, Grenoble, France
- ³⁹ Laboratoire de l'Accélérateur Linéaire, Université Paris-Sud 11, CNRS/IN2P3, Orsay, France
- ⁴⁰ Lawrence Berkeley National Laboratory, Berkeley, California, U.S.A.
- ⁴¹ Max-Planck-Institut für Astrophysik, Karl-Schwarzschild-Str. 1, 85741 Garching, Germany
- ⁴² National University of Ireland, Department of Experimental Physics, Maynooth, Co. Kildare, Ireland
- ⁴³ Observational Cosmology, Mail Stop 367-17, California Institute of Technology, Pasadena, CA, 91125, U.S.A.
- ⁴⁴ Optical Science Laboratory, University College London, Gower Street, London, U.K.
- ⁴⁵ Rutherford Appleton Laboratory, Chilton, Didcot, U.K.
- ⁴⁶ SUPA, Institute for Astronomy, University of Edinburgh, Royal Observatory, Blackford Hill, Edinburgh EH9 3HJ, U.K.
- ⁴⁷ School of Physics and Astronomy, Cardiff University, Queens Buildings, The Parade, Cardiff, CF24 3AA, U.K.
- ⁴⁸ Space Research Institute (IKI), Russian Academy of Sciences, Profsoyuznaya Str, 84/32, Moscow, 117997, Russia
- ⁴⁹ Space Sciences Laboratory, University of California, Berkeley, California, U.S.A.
- ⁵⁰ Stanford University, Dept of Physics, Varian Physics Bldg, 382 Via Pueblo Mall, Stanford, California, U.S.A.
- ⁵¹ Universität Heidelberg, Institut für Theoretische Astrophysik, Albert-Überle-Str. 2, 69120, Heidelberg, Germany
- ⁵² Université de Toulouse, UPS-OMP, IRAP, F-31028 Toulouse cedex 4, France
- ⁵³ Universities Space Research Association, Stratospheric Observatory for Infrared Astronomy, MS 211-3, Moffett Field, CA 94035, U.S.A.
- ⁵⁴ University of Cambridge, Cavendish Laboratory, Astrophysics group, J J Thomson Avenue, Cambridge, U.K.
- ⁵⁵ University of Cambridge, Institute of Astronomy, Madingley Road, Cambridge, U.K.
- ⁵⁶ University of Cambridge/Astrophysics, Group Madingley, Road CB3 0HE, Cambridge, U.K.
- ⁵⁷ University of Granada, Departamento de Física Teórica y del Cosmos, Facultad de Ciencias, Granada, Spain
- ⁵⁸ University of Miami, Knight Physics Building, 1320 Campo Sano Dr., Coral Gables, Florida, U.S.A.
- ⁵⁹ Warsaw University Observatory, Aleje Ujazdowskie 4, 00-478 Warszawa, Poland